



**HAL**  
open science

## Hydrogen adsorption on Ni-functionalized saponites and their precursor gel

L Masci, Laurent Truche, Valérie Magnin, Martine Lanson, A Moya, Patricia de Rango, N Finding, Lanson Bruno, A Viola, Jonathan Deseure, et al.

► **To cite this version:**

L Masci, Laurent Truche, Valérie Magnin, Martine Lanson, A Moya, et al.. Hydrogen adsorption on Ni-functionalized saponites and their precursor gel. International Journal of Hydrogen Energy, 2024, 58, pp.79-92. 10.1016/j.ijhydene.2023.10.314 . hal-04186726

**HAL Id: hal-04186726**

**<https://hal.science/hal-04186726>**

Submitted on 24 Aug 2023

**HAL** is a multi-disciplinary open access archive for the deposit and dissemination of scientific research documents, whether they are published or not. The documents may come from teaching and research institutions in France or abroad, or from public or private research centers.

L'archive ouverte pluridisciplinaire **HAL**, est destinée au dépôt et à la diffusion de documents scientifiques de niveau recherche, publiés ou non, émanant des établissements d'enseignement et de recherche français ou étrangers, des laboratoires publics ou privés.

# Hydrogen adsorption on Ni-functionalized saponites and their precursor gel.

<sup>1</sup>Masci L., <sup>1</sup>Truche L., <sup>1</sup>Magnin V., <sup>1</sup>Lanson M., <sup>2</sup>De Rango P., <sup>1</sup>Moya A., <sup>1</sup>Findling N., <sup>1</sup>Lanson B.,  
<sup>3</sup>Viola A., <sup>3</sup>Deseure J., <sup>4</sup>Abdel Sater M., <sup>4</sup>Launois P., <sup>5</sup>Joubert G., <sup>5</sup>Toubon H.

<sup>1</sup>*Univ. Grenoble Alpes, Univ. Savoie Mont Blanc, CNRS, IRD, Univ. Gustave Eiffel, ISTERre, 38000 Grenoble, France*

<sup>2</sup>*Univ. Grenoble Alpes, CNRS, Institut Néel, 38000 Grenoble, France*

<sup>3</sup>*University Grenoble Alpes, University Savoie Mont Blanc, CNRS, Grenoble INP (Institute of Engineering and Management University Grenoble Alpes), LEPMI, 38000 Grenoble, France*

<sup>4</sup>*Laboratoire de Physique des Solides, CNRS, Université Paris-Saclay, F-91405 Orsay, France*

<sup>5</sup>*ORANO, 125 Av. de Paris, 92320 Châtillon, France*

## ABSTRACT

Here we propose to investigate Ni-functionalized saponite (smectite group) as a viable alternative for low cost H<sub>2</sub> storage for land-based applications. The precursor gel used for saponite synthesis is also tested with respect to its H<sub>2</sub> adsorption properties. Adsorption isotherms recorded at 77 K and 1 bar, 298 K and 120 bar indicate that nickel functionalization does not induce a clear structural or chemical control on the adsorption process. However, Ni-pillared saponites outgassed at 70 °C display a four-time enhanced H<sub>2</sub> uptake (up to 0.12 wt% at 77 K and 1 bar) compared to its counterpart outgassed at 150 °C. Another important finding of this study is the surprisingly high H<sub>2</sub> uptakes of the gel (nano-crystallized) precursor, used for the synthesis of saponite samples (up to 0.19 wt% at 77 K and 1 bar, and up to 0.12 wt% at 298 K and 120 bar).

## 23 KEY-WORDS

24 Clay materials, saponite, H<sub>2</sub> adsorption, isotherms, specific surface area, Ni functionalization,  
25 hydrogen storage

## 26 1. Introduction

27 This last decade has seen an increase of interest for hydrogen (H<sub>2</sub>) as a carbon free energy  
28 vector that can be stored. If produced by water electrolysis from renewable energy, or from  
29 fossil fuels with carbon capture and sequestration, this molecule is a good candidate to replace  
30 fossil fuels, for both mobile and stationary applications, because of its high energy density per  
31 mass unit (142 MJ/kg) [1–3]. However, one of hydrogen main drawbacks lies in its low  
32 volumetric density at ambient temperature and pressure, which requires specific storage  
33 technologies. Besides conventional storage methods such as high-pressure gas reservoirs (up  
34 to 700 bar at ambient temperature), cryo-compression (supercritical H<sub>2</sub> at 23 K and ~ 300 bar),  
35 or metal hydrides (H<sub>2</sub> chemisorption, where the T - P range depends on the chosen metal  
36 hydride: typically 25 < T < 300 °C and 1 < P < 10 bar), many solid porous media have been  
37 developed to store H<sub>2</sub> through physisorption interactions.

38 Among these materials, Metal Organic Frameworks (MOFs), zeolites, carbon-based nano  
39 materials have been thoroughly investigated for their hydrogen gravimetric density (i.e.  
40 kg<sub>H<sub>2</sub></sub>/kg<sub>material</sub>) reaching up to ~ 9 wt% H<sub>2</sub> at 77 K and 50 bar for these compounds [4–11].  
41 Nevertheless, these materials have several disadvantages such as high production costs [12],  
42 complex manufacturing processes [13], low stabilities [14], and high toxicities inherent to their  
43 chemical composition and nanostructure [15]. Even more important, hydrogen storage  
44 materials based on physisorption process suffer from a dramatic loss of storage capacity as

1  
2  
3  
4  
5  
6  
7  
8  
9  
10  
11  
12  
13  
14  
15  
16  
17  
18  
19  
20  
21  
22  
23  
24  
25  
26  
27  
28  
29  
30  
31  
32  
33  
34  
35  
36  
37  
38  
39  
40  
41  
42  
43  
44  
45 temperature increases above 77 K due to the low enthalpy of H<sub>2</sub> adsorption on these  
46 materials, i.e. 5 - 8 kJ/mol [16]. The adsorption capacity of carbon-based nanomaterials  
47 typically decreases by one order of magnitude from 77 K to 298 K. For example, H<sub>2</sub> uptake of  
48 single-wall carbon nanotubes is ~ 2 wt% H<sub>2</sub> at 77 K and 40 bar, but decreases down to ~ 0.2  
49 wt% H<sub>2</sub> at 298 K and 200 bar [11].

50 Clay minerals, like smectites, illites or kaolinites, display interesting H<sub>2</sub> adsorption properties  
51 and help to overcome some of the above-mentioned limitations. Smectites in particular are  
52 promising materials thanks to their abundance in natural environments, their ease of mass  
53 production, their large surface area and their high sorption capacities with respect to a  
54 plethora of gases, molecules and dissolved ions. Smectites are formed by a 2:1 layer made of  
55 an octahedral sheet filled by Mg<sup>2+</sup> cations, in between two tetrahedral sheets (also called TOT  
56 layers) filled with Si<sup>4+</sup> and Al<sup>3+</sup> cations in the case of saponite (see Fig. 1a). The charge deficit  
57 induced by the replacement of Si<sup>4+</sup> by Al<sup>3+</sup>, is compensated by interlayer cations, here, Na<sup>+</sup> or  
58 Ca<sup>+</sup>. The intercalation of H<sub>2</sub> in the interlayer space, may be favored by: i) strong electrostatic  
59 interactions inside the interlayer cavities due to the presence of exchangeable cations (this  
60 electrostatic field induces a dipolar moment to H<sub>2</sub> - nominally apolar - and thus promotes its  
61 physisorption), ii) the geometry of the interlayer space which is homogeneous and does not  
62 present bottleneck likely to prevent H<sub>2</sub> diffusion, and iii) the size of the interlayer micropore  
63 network that can match a few H<sub>2</sub> diameter (2.89 Å) [17]. Hydrogen may also be adsorbed on  
64 the basal and edge sites, and in the porosity in between clay particles. The high specific surface  
65 area (SSA) of clay minerals, that can reach ~ 400 m<sup>2</sup>/g for some particular clays such as  
66 laponite® [17–19], also make them good sorbents for gases like CO<sub>2</sub> and CH<sub>4</sub> [20–24].

67 Yet, H<sub>2</sub> adsorption capacity of smectites and other clay minerals remains poorly investigated.

68 A maximum gravimetric sorption capacity of ~ 0.2 wt% H<sub>2</sub> was recorded at 77 K and ~ 1 bar H<sub>2</sub>

69 pressure for Al-pillared montmorillonite [25], K-bentonite [26] and sepiolite [27]. Edge and

70 Edge et al. [17,28] studied several varieties of laponite<sup>®</sup>, which is a registered trademark for a

71 type of smectite , and measured H<sub>2</sub> uptake as a function of temperature and pressure. They

72 reported maximum sorption capacity of ~ 0.1 wt% H<sub>2</sub> at ambient temperature and 140 bar,

73 and up to 0.63 wt% H<sub>2</sub> at 1 bar and 77 K. Recently, Ziemiański & Derkowski [29] investigated

74 H<sub>2</sub> adsorption on montmorillonite and illite at temperatures ranging from 25 °C to 70 °C and

75 pressure up to 145 bar. They concluded that H<sub>2</sub> intercalation within smectite interlayers is

76 strongly dependent on hydration state of the interlayer space, itself controlled by the nature

77 of the exchangeable cation. Under the tested conditions the maximum H<sub>2</sub> uptake never

78 exceeded 0.04 wt%, even if montmorillonite exchanged with tetramethylammonium cation

79 was a noticeable exception displaying an H<sub>2</sub> uptake of 0.1 wt% at 25 °C and 145 bar.

80 At 77 K, high H<sub>2</sub> sorption values on clays and other porous media are well correlated to the

81 specific surface areas and the micropore volume [27,30,31]. However, it remains unclear

82 whether clay minerals micropores suitable for H<sub>2</sub> adsorption are localized inside the interlayer

83 space, on the edges of the 2:1 layer, on the basal surfaces, or in-between the particles. In

84 addition, the ability of the interlayer space to incorporate gases such as CO<sub>2</sub> strongly depends

85 on both the hydration state, and the nature of the charge-balancing cations [23]. The effect

86 of water content is significant as it might control the space available for gas species adsorption

87 and compete with the sorbent gas. Many studies on clays managed to optimize the interlayer

88 space, by addition of molecular species such as transition metal cations or organic molecules

89 [32–34]. To that extent, pillared clays are the most common type of functionalized clay-based

1  
2  
3  
4  
5  
6  
7  
8  
9  
10  
11  
12  
13  
14  
15  
16  
17  
18  
19  
20  
21  
22  
23  
24  
25  
26  
27  
28  
29  
30  
31  
32  
33  
34  
35  
36  
37  
38  
39  
40  
41  
42  
43  
44  
45  
46  
47  
48  
49  
50  
51  
52  
53  
54  
55  
56  
57  
58  
59  
60  
61  
62  
63  
64  
65

90 materials as their interlayer space is modified on purpose to create a porous network suitable  
91 to enhance the adsorption of a given molecule [25,35–38].  
92 In addition to the effect of porosity, several studies on porous materials highlighted the  
93 effectiveness of transition metals such as nickel, in increasing the electrostatic field able to  
94 attract and polarize hydrogen atoms on diverse material surfaces [39–41]. Beyond its low cost,  
95 compared to classically used H<sub>2</sub>-catalysts, like platinum or palladium metals, nickel is a natural  
96 component of various types of clays [42,43], and may occupy different crystallographic sites  
97 in the clay structure.  
98 As questions remain open on the links between clays porosity and their H<sub>2</sub> adsorption  
99 capacity, we focused on the structural properties of a synthetic saponite in order to decipher  
100 the crystal-chemical influence on H<sub>2</sub> physisorption. Several saponite were thus synthesized  
101 with a carefully controlled addition of Ni<sup>2+</sup> cations or Ni<sup>0</sup> nano-particles to the structure at  
102 different potential H<sub>2</sub> adsorption sites (i.e. interlayer space, edges, basal surface, and  
103 octahedral sites) in order to probe the adsorption properties of these sites. In addition, the  
104 precursor gel used for saponite synthesis was also tested with respect to its H<sub>2</sub> adsorption  
105 properties.

## 106 107 **2. Materials and methods**

### 108 **2.1 Sample description**

#### 109 **2.1.1 Ni-functionalized saponites**

with a layer charge of 1.2 e<sup>-</sup> per O<sub>20</sub>(OH)<sub>4</sub>

Name	S <sub>BET</sub> m <sup>2</sup> /g	S <sub>μporous</sub> m <sup>2</sup> /g	V <sub>μporous</sub> cm <sup>3</sup> /g	H <sub>2</sub> uptake		Description
				77 K-1 bar	298 K-120 bar	
				wt% H <sub>2</sub>		
<b>CLAYS</b>						
Sap1.2	31	0	0	0.02	0	Ni-free saponite with a charge layer of 1.2
Sap1.2_Ni-interl.	35	0	0	0.02	-	Na <sup>+</sup> exchanged with Ni <sup>2+</sup> inside the interlayer space
Sap1.2_Ni-pillars	37	2	0.001	0.01	0	Ni(OH) <sub>2</sub> pillars inside the interlayer space
Sap1.2_Ni-edges1	37	3	0.001	0.03	0	Ni <sup>2+</sup> sorbed on the edges for 2 h
Sap1.2_Ni-edges2	40	6	0.003	0.01	-	Ni <sup>2+</sup> sorbed on the edges for 12 h
Sap1.2_Ni-edges3	37	2	0.001	0.03	0	Ni <sup>2+</sup> sorbed on the edges for 22 days
Sap1.2_Ni-surface	9	0	0	0.01	-	Ni <sup>0</sup> nanoparticles on surface
Gel_Sap1.2	145	77	0.029	0.19	0.12	Precursor gel
<b>STANDARDS</b>						
MOF-177	3856	3835	1.547	1.22	0.51	
<i>Furukawa et al., 2007</i>	4630	n.a.	n.a.	1.25*	n.a.	
<i>Li and Yang, 2007</i>	3100	n.a.	n.a.	1.50	n.a.	
<i>Voskuilen et al., 2012</i>	4126	n.a.	1.67	n.a.	0.55	
<i>Zacharia et al., 2010</i>	3400 - 4100**	n.a.	1.3 - 1.6	n.a.	0.59	
Activated Carbon	872	523	0.213	1.38	-	
Y-Zeolite	677	630	0.242	0.03	-	
LapRD	347	340	0.239	0.26	0.12	
<i>Edge, 2014</i>	399***			0.24	~ 0.11	
- not measured						
n.a. not available						
* measured at 0.8 bar						
** for densities d = 0.39 - 0.51						
*** calculated from DFT calculations						
Caption: H <sub>2</sub> modeling applied to H <sub>2</sub> isotherms realized at 77 K						

110

111 **Table 1.** Description and summary of textural parameters (S<sub>BET</sub>, S<sub>μporous</sub>, V<sub>μporous</sub>) and H<sub>2</sub> uptake for all  
 112 clay materials from this study (*Sap1.2*, Ni-saponites, and *Gel\_Sap1.2*), and for standards used in this  
 113 study and from the literature [17,31,44–46].

114 Saponite with the structural composition Si<sub>8-X</sub>Al<sub>X</sub>Mg<sub>6</sub>O<sub>20</sub>(OH)<sub>4</sub>Na<sub>X</sub>, a layer charge deficit X =  
 115 1.2 (sample named as *Sap1.2*) and a density of d ~ 2.3 g/cm<sup>3</sup> [47] was initially synthesized as a  
 116 template for Ni functionalization (see protocol at the next section). Two Ni-saponite samples  
 117 were synthesized by addition of Ni<sup>2+</sup> into the interlayer space. The first sample, named  
 118 *Sap1.2\_Ni-interl.*, has the structural composition Si<sub>6.8</sub>Al<sub>1.2</sub>Mg<sub>6</sub>O<sub>20</sub>(OH)<sub>4</sub>Ni<sub>0.6</sub> with hydrated Ni<sup>2+</sup>  
 119 replacing interlayer Na<sup>+</sup> cations. The second configuration, named *Sap1.2\_Ni-pillars*,  
 120 corresponds to the formation of Ni(OH)<sub>2</sub> pillars, creating a porous network inside the  
 121 interlayer space that is supposed to prevent its complete collapse during thermal treatments  
 122 prior to volumetric analysis [37]. In addition, three different Ni-saponite samples with Ni<sup>2+</sup>  
 123 located on the edges were also prepared. According to available protocols [48,49], various

124 duration of sorption experiments led to three samples with different extent of Ni octahedral  
125 sheet on particle outer edges : i) with Ni<sup>2+</sup> cations only adsorbed on the edges of the TOT layer,  
126 named *Sap1.2\_Ni-edges1*, ii) with partial recrystallization of octahedral and tetrahedral sites  
127 from the edges, and Ni<sup>2+</sup> incorporation into the new octahedral sites, named *Sap\_Ni-edges2*,  
128 and iii) with complete structural Ni<sup>2+</sup> recrystallization, named *Sap1.2\_Ni-edges3*. An additional  
129 configuration was tested by addition of Ni<sup>0</sup> nanoparticles deposited on the surface of *Sap1.2*  
130 sheets, and is called *Sap1.2\_Ni-surface*. All atomic structures of saponites are shown in Fig. 1,  
131 and listed in Table 1. The gel precursor used for the hydrothermal synthesis of Na-saturated  
132 saponite, named *Gel\_Sap1.2*, was also analysed for its H<sub>2</sub> adsorption properties. The apparent  
133 density of the gel was measured volumetrically and was found to be around 1.0 g/cm<sup>3</sup>.  
134 All syntheses and analytical measurements were carried out at ISTerre laboratory (Grenoble,  
135 France), excepted if clearly mentioned.

136

137



Figure 1

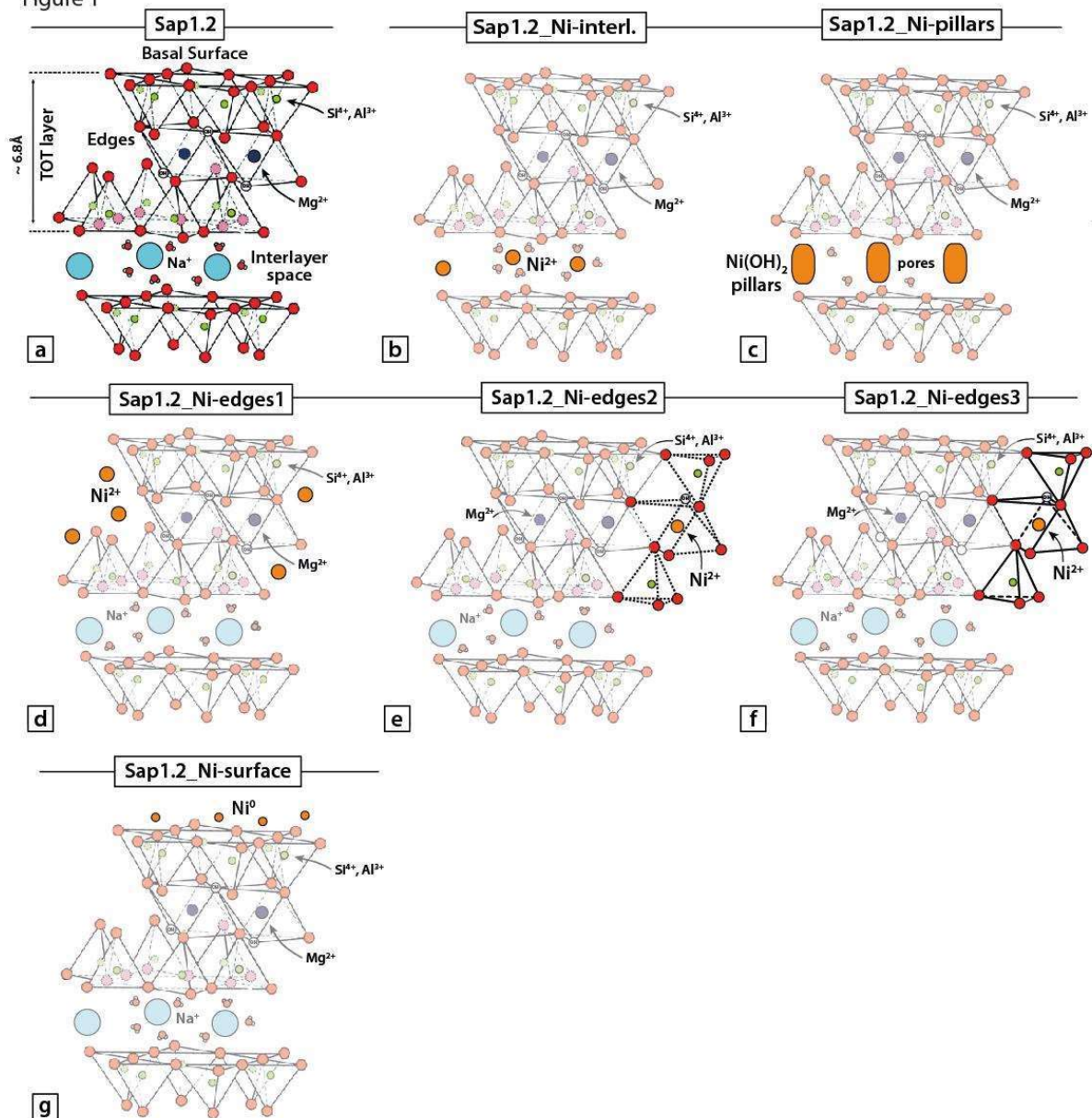


**Fig. 1.** Crystal-chemical configurations of saponites with Ni addition to the structure (basic structure modified with permission from Paineau et al. [50], after Grim et al. [51]). They are described as followed: a) saponite Na-saturated sample (*Sap1.2*); b) and c) saponites whose interlayer space was modified with Ni<sup>2+</sup> cations sorption (*Sap1.2\_Ni-interl.*), or Ni(OH)<sub>2</sub> pillaring (*Sap1.2\_Ni-pillars*); d) to f) saponites whose edges were modified with Ni<sup>2+</sup> sorption (*Sap1.2\_Ni-edge1*), partial crystallization (*Sap1.2\_Ni-edge2*), or complete crystallization of Ni<sup>2+</sup> into new octahedral sites (*Sap1.2\_Ni-edge3*); g) saponite whose surface was modified by sorption of Ni<sup>0</sup> nanoparticles (*Sap1.2\_Ni-surface*).

### 2.1.2 Standards

In addition to saponites, several porous materials previously described in the literature have been characterized as N<sub>2</sub> and H<sub>2</sub> adsorption standards to validate our volumetric measurements protocol. A Metal-Organic Framework (*MOF-177*, CAS number 676593-65-0, density  $d = 0.35 \text{ g/cm}^3$ ) and an activated carbon (*Activated carbon*, CAS number: 7440-44-0) were purchased from Sigma-Aldrich®. Finally, a zeolite (*Y-zeolite*) was provided by Micromeritics® as an internal standard for N<sub>2</sub> volumetric measurements, and a commercial laponite® (*LapRD*) obtained from Laporte PLC® (ref: 5765) was also used.

### 2.2 Experimental protocol

Synthesis of saponite (*Sap1.2*) was carried out using hydrothermal method from a sol gel solution according to a well-established protocol [35,52,53]. The precursor gel (*Gel\_Sap1.2*) was prepared from saturated Mg(NO<sub>3</sub>)<sub>2</sub> and Al(NO<sub>3</sub>)<sub>3</sub> solutions, Na<sub>2</sub>CO<sub>3</sub>, and Tetra Ethyl Ortho Silicate (TEOS) solutions as Mg, Al, Na and Si sources, respectively, in proportions corresponding to the stoichiometric formula. The saponite synthesis was achieved at 400 °C and 400 bar of water confining pressure during 4 weeks using an externally heated Morey-type pressure vessel fitted with an internal silver tubing containing 8 g of *Gel\_Sap1.2*. After the hydrothermal synthesis, saponite sample was Na-saturated by mixing 1 mol/L aqueous solution of NaCl with saponite for 24 h before separation of the solid fraction by centrifugation (1 cycle of 10 min at 9000 rpm). Excess NaCl was removed by rinsing the solid 4 times with deionized water followed by steps of centrifugation to isolate the solid fraction (4 cycles of 10 min at 12000 rpm).

Part of the resulting crystallized *Sap1.2* was afterwards mixed with a solution of NiCl<sub>2</sub> at 0.2 mol/L and matured during 2 x 45 min at ambient temperature, leading to the *Sap1.2\_Ni-interl.*

169 The *Sap1.2\_Ni-pillars* was obtained using an annealing route: an aliquot of *Sap1.2\_Ni-interl.*  
170 suspension was placed into a 23 mL Parr vessel with NaOH solution at  $10^{-5}$  mol/L at 80 °C for  
171 12 days. As a result, Ni(OH)<sub>2</sub> pillars, i.e. isolated “island-like” fragments of a Ni(OH)<sub>2</sub> octahedral  
172 sheet, were crystallized inside the interlayer space.

173 *Sap1.2\_Ni-edges1,2,3* samples were prepared from solutions mixed with milli-Q® water  
174 (conductivity of 18.2 MOhm.cm) and chemicals of ACS reagent grade. The synthesis was  
175 conducted in a thermostated glass vessel at 25 °C with constant stirring of the suspension at  
176 250 rpm. An inert atmosphere was maintained by bubbling Ar purified by a solutions setup  
177 (H<sub>2</sub>SO<sub>4</sub> 0.1 M, NaOH 0.1 M and NaCl 0.25 M). 100 mL of *Sap1.2* suspension at 9.1 g/L was  
178 added to 39 mL milli-Q water in which 2.118 g of NaCl salt has been previously dissolved in  
179 order to obtain a high ionic strength and to saturate the interlayer space with Na<sup>+</sup>. Finally, 1  
180 mL of SiO<sub>2</sub> solution at 0.0725 M was added to compensate the *Sap1.2* dissolution and to allow  
181 the epitaxial growth on the edges of the saponite layers [48]. The pH was adjusted and  
182 maintained at 7.3 by automated NaOH (0.02 M) addition using a Metrohm® 716 DMS device  
183 running with Tiamo™ software. After pH equilibration for 5 hours, 5 mL of a solution containing  
184 NiCl<sub>2</sub> at 23.8 mM and NaCl at 0.25 M was added. The final suspension has a solid-to-liquid  
185 ratio of 6.3 g/L, a Ni aqueous concentration of 820 μM, a Si<sub>aq</sub> concentration of 500 μM and a  
186 high ionic strength (NaCl) 0.25 M. Afterwards, three samples of 50 mL of this suspension were  
187 collected at 2h, 22h and 22 days. Each sample was filtered through a 0.1 μm nitrocellulose  
188 filter, washed twice with milli-Q® water and then freeze-dried.

189 Saponite decoration with Ni<sup>0</sup> nanoparticles (*Sap1.2\_Ni-surface*) was carried out *via* polyol  
190 method at LEPMI laboratory (Grenoble, France). Ni<sup>0</sup> nanoparticles were generated from the  
191 reduction of dissolved Ni salt in the presence of the *Sap1.2* dispersed in ethylene glycol (EG)  
192 that acts as solvent, reducing agent and stabilizer. Addition of monosodium citrate as

193 surfactant allows to better control the size of the particles. In details, 890 mg of  $\text{NiCl}_2 \cdot 6\text{H}_2\text{O}$   
194 and 1.180 g of monosodium citrate were mixed in 100 mL EG in a 250 mL flask. After complete  
195 dissolution of the salts, pH was adjusted to 10 by dropwise addition of a 5 wt% solution of  
196 KOH in EG. After addition of 175 mg of previously synthesized *Sap1.2*, the mixture was heated  
197 under gentle stirring to 160 °C for 20 hours. After cooling down to room temperature, the final  
198 product was collected by centrifugation (9000 rpm – 20 min), rinsed several times with  
199 deionized water, and dried at 60 °C for 1 hour.

### 2.3 X-ray diffraction

201 XRD patterns were recorded on powders using a Bruker D8 diffractometer operated in the  
202 Bragg-Brentano geometry at 40 kV and 40 mA, and equipped with a SolX Si(Li) solid state  
203 detector from Baltic Scientific Instruments®. Intensities were recorded at 0.04° 2 $\theta$  step  
204 intervals from 2 to 20° 2 $\theta$  range (6 s counting time per step –  $\text{CuK}\alpha_{1+2}$  radiation). The  
205 diffractometer was also equipped with a MHG Messtechnik® humidity controller coupled to  
206 an Anton Paar® CHC+ chamber, to perform analyses at various relative humidities (RH = 3%,  
207 10% and 80%).

208 Powder X-ray diffraction for *Sap1.2* and *Gel\_Sap1.2* was also carried out on the MORPHEUS  
209 platform of Laboratoire de Physique des Solides (Orsay, France) using a copper rotating anode  
210 (RU H3R, Rigaku Corp., Japan) operating at a wavelength  $\lambda = 0.1542$  nm delivered by Osmic  
211 optics. The diffractometer is equipped with a two-dimensional mar345 detector (marXperts  
212 GmbH, Germany) with 150  $\mu\text{m}$  pixel size, placed at 150 mm from the sample: glass capillary (1  
213 mm diameter) filled with powder material (saponite or gel). It has been heated inside a  
214 furnace at 150 °C for 6 hours under primary vacuum conditions and then sealed. The two-  
215 dimensional diffraction patterns consist in concentric rings with constant angular intensity.

216 Background signals from air and from the capillary are subtracted based on the measurement  
217 of the absorption of the direct beam by the sample. The measured intensity is also corrected  
218 from the geometrical factor to be used for a planar detector, the polarisation factor and the  
219 X-ray absorption between the sample and a given pixel on the detector.

## 220 **2.4 N<sub>2</sub> and H<sub>2</sub> adsorption experiments**

221 Unless specifically mentioned, all materials were initially degassed at 150 °C for 6 h under real  
222 secondary vacuum at  $4 \times 10^{-3}$  mbar. Nitrogen and hydrogen physisorption experiments were  
223 carried out at 1 bar and 77 K, using a volumetric gas sorption instrument ASAP 2020 PLUS from  
224 Micromeritics Instruments®. From N<sub>2</sub> isotherms, the specific surface area of powdered  
225 samples (150 - 500 mg) was estimated using the Brunauer–Emmet–Teller ( $S_{\text{BET}}$ ) equation in  
226 the  $0.05 \leq P/P_0 \leq 0.3$  interval of relative pressure and using a cross-sectional area of  $16.2 \text{ \AA}^2$   
227 for molecular N<sub>2</sub>. For microporous samples, the free space measurements were performed by  
228 a BET analysis until  $P/P_0 = 0.4$ , before outgassing again the samples to prevent He retention  
229 previously used for dead volume measurement. Data analyses were performed using ASAP  
230 2020 Plus software from Micromeritics®. The presence of micropores in the sample ( $\phi_{\text{pore}} < 2$   
231 nm) was assessed using the t-plot method [54].

232 Hydrogen isotherms were acquired with an equilibration interval of 60 seconds for routine  
233 analysis (~ 5 to 8 hours for a complete isotherm acquisition). An ultra-high purity grade of H<sub>2</sub>  
234 (99.999% purity) was used for the adsorption experiments.

235 High pressure hydrogen experiments were performed at 298 K and 120 bar at the Neel  
236 Institute using a PCT Hiden® IMI system apparatus and data analyses were performed using  
237 Isochema® software. Around 200 to 600 mg of powdered samples were inserted inside a steel  
238 sample holder (internal volume ~ 200 mm<sup>3</sup>), with a small amount of glass wool to prevent

239 powder removal during vacuuming steps. Adsorption and desorption isotherms were  
240 performed with an equilibration time of 15 - 30 minutes for routine analysis. As for low  
241 pressure analysis, each sample was heated and outgassed at 150 °C for at least 6 hours prior  
242 to each measurement.

## 243 **2.5 Thermogravimetric analyses (DSC-TGA)**

244 TG/DSC curves were recorded on a TGA/DSC3+ Mettler Toledo® instrument. Approximately  
245 50 mg of sample (+/- 30 mg) were placed in a 150 µL alumina crucible. The experiments were  
246 carried out under N<sub>2</sub> atmosphere with a flow rate of 20 mL/min. Sample mass loss and  
247 associated thermal effects were recorded from 25 to 900 °C using a constant heating ramp of  
248 5 °C/min. In order to identify the different mass loss steps, the TGA first derivative (rate of  
249 mass loss) was used.

## 250 **2.6 Atomic Force Microscopy (AFM)**

251 Atomic Force Microscopy (AFM) measurements were conducted to measure *Sap1.2* particles  
252 topography and particles size. The device used was a MFP-3D microscope with contact mode  
253 from Asylum Research® (Santa Barbara, USA). The maximum range of the piezo scanner is 120  
254 µm in the planar direction (x,y) and 15 µm in the vertical direction (z). The microscope is  
255 isolated inside a chamber and mounted on top of a vibration isolation control unit from  
256 Herzan®. Topography images were acquired in contact mode using triangular silicon nitride  
257 (PNP-TR from NanoWorld®) cantilevers with a nominal length of 200 µm, width of 28 µm and  
258 a thickness of 500 nm. Before each experiment, the deflection sensitivity was determined and  
259 the spring constants were routinely calibrated using the thermal method, resulting in 100-200  
260 pN/nm. The obtained data were processed using the AR and WSxM softwares [55].

261 Prior to AFM measurement, sample of *Sap1.2* was deposited on mica substrate. First, the  
262 powder was dispersed in Milli-Q® water (1 mg/mL) and 100 µL of the solution was deposited  
263 on the mica plate, dried at room temperature for 1 hour and blown with N<sub>2</sub>.

## 264 **2.7 Transmission Electron Microscopy imaging (TEM)**

265 Transmission Electron Microscopy images were acquired using a Jeol® 2010 microscope  
266 (CMTC-INPG) with a LaB<sub>6</sub> filament and operating at 200 kV. The images were collected with a  
267 2048 × 2048 pixels CCD camera (Gatan® Ultrascan 1000 XP).

## 269 **3. Results**

### 270 **3.1 XRD results**

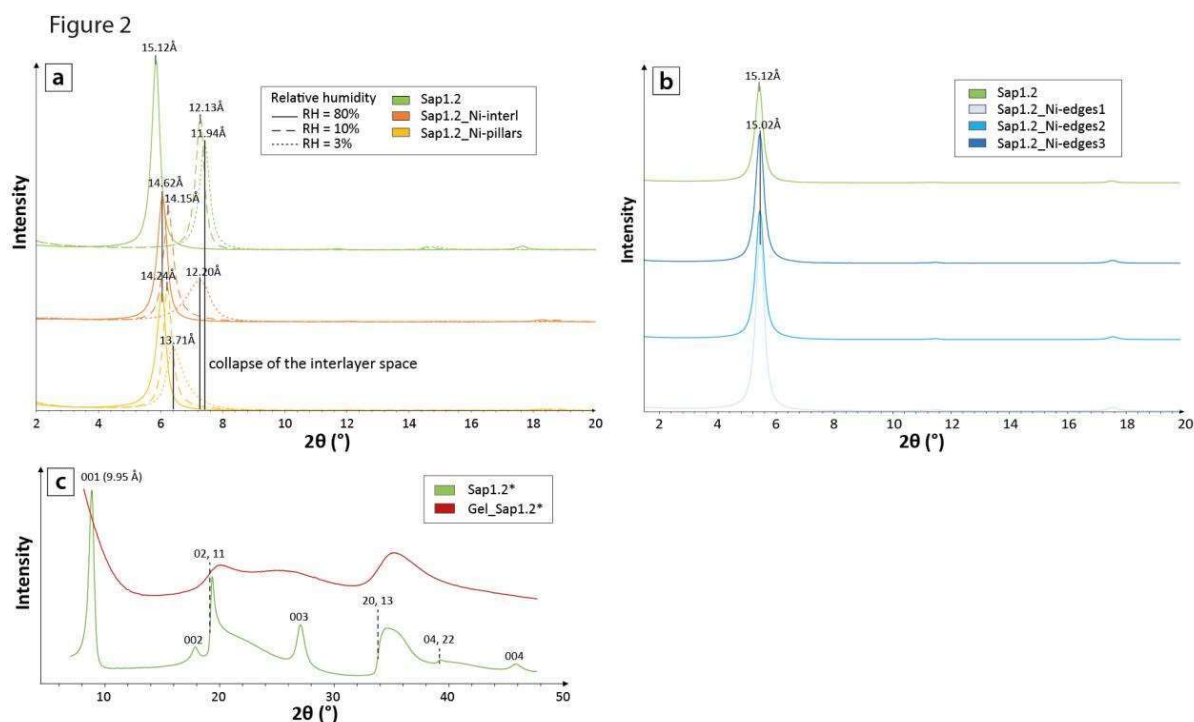
271 XRD measurements on Ni-saponites whose interlayer space was modified with Ni<sup>2+</sup> exchange  
272 (*Sap1.2\_Ni-interl.*) or pillaring (*Sap1.2\_Ni-pillars*) are displayed in Fig. 2a. At RH = 80%, Ni  
273 intercalation in the structure implies a slight shift of the apparent  $d_{001}$ -spacing from 15.12 Å  
274 to 14.62 Å and 14.24 Å for cations exchange or pillaring in the interlayer respectively,  
275 compared to the initial Na-saturated *Sap1.2*. Without pillaring, decreasing RH from 80 to 10%,  
276 induces noticeable difference between Na-saturated (*Sap1.2*) and Ni<sup>2+</sup> exchanged saponite  
277 (*Sap1.2\_Ni-interl.*). One can observe that Ni<sup>2+</sup> has a higher water affinity than Na<sup>+</sup>, as  
278 *Sap1.2\_Ni-interl.* apparent  $d_{001}$ -spacing is still at 14.15 Å at RH = 10%, while the apparent  $d_{001}$ -  
279 spacing of *Sap1.2* has already decreased to 12.13 Å, consistently with previous results [56].  
280 Further drying of *Sap1.2\_Ni-interl.* down to RH = 3% leads to a marked decrease of the  
281 apparent  $d_{001}$ -spacing from 14.15 Å to 12.20 Å. This phenomenon is due to partial interlayer  
282 cation dehydration. Slight differences do exist when Na<sup>+</sup> is exchanged by Ni<sup>2+</sup> in the interlayer.

283 This is shown by apparent  $d_{001}$ -spacing at RH = 3% of 11.94 Å and 12.20 Å for *Sap1.2* and  
284 *Sap1.2\_Ni-interl.*, respectively (Fig. 2a). Dehydration phenomenon has only a minor effect on  
285 *Sap1.2\_Ni-pillars*, whose apparent  $d_{001}$ -spacing is 14.24 Å at RH = 80% and 13.71 Å at RH = 3%,  
286 confirming the presence of Ni(OH)<sub>2</sub> pillars in the interlayer space. Indeed the presence of these  
287 pillars prevents the collapse of the interlayer as previously reported [57].

288 Saponites whose edges were modified by nickel addition (i.e. *Sap1.2\_Ni-edges1,2,3*) evidence  
289 almost no apparent  $d_{001}$ -spacing shift compared to *Sap1.2* at RH = 80%, with  $d = 15.02$  Å for  
290 the three samples and  $d = 15.12$  Å for *Sap1.2* (Fig. 2b). This observation confirms incorporation  
291 (adsorbed or incorporated) of Ni<sup>2+</sup> cations on the edges and not inside the interlayer space. In  
292 Fig. 2a and 2b, only the 00 $l$  reflections are observed due to the geometry of the experiment  
293 and the use of oriented preparations.

294 The powder X-ray diffractogram of *Sap1.2* is shown in Fig. 2c. One observes the 00 $l$  reflections  
295 characteristic of the coherent stacking of the TOT sheets. In addition,  $hk$  bands with typical  
296 sawtooth profiles are observed rather than  $hkl$  reflections owing to turbostratism (systemic  
297 occurrence of stacking disorder in between successive layers). The in-plane coherence lengths  
298 are given by the slope of the rising edge of the bands [58]. It is resolution limited here, which  
299 only allows us to conclude that they are larger than a few tens of nanometer. The 02,11 and  
300 20,13 bands are still visible for *Gel\_Sap1.2*, with a much smoother rising edge however,  
301 indicative of very small fragments of octahedral/tetrahedral sheets constitutive of TOT layers,  
302 and representative of a nano-crystallized component. An additional broad and symmetric  
303 hump centered at  $2\theta \approx 25^\circ$  is also observed, which may correspond to an amorphous gel  
304 component. No 001 peak is observed, due to the intense signal at small angles reflecting the  
305 porosity of the assembly of these small solid particles (Fig. 2c).





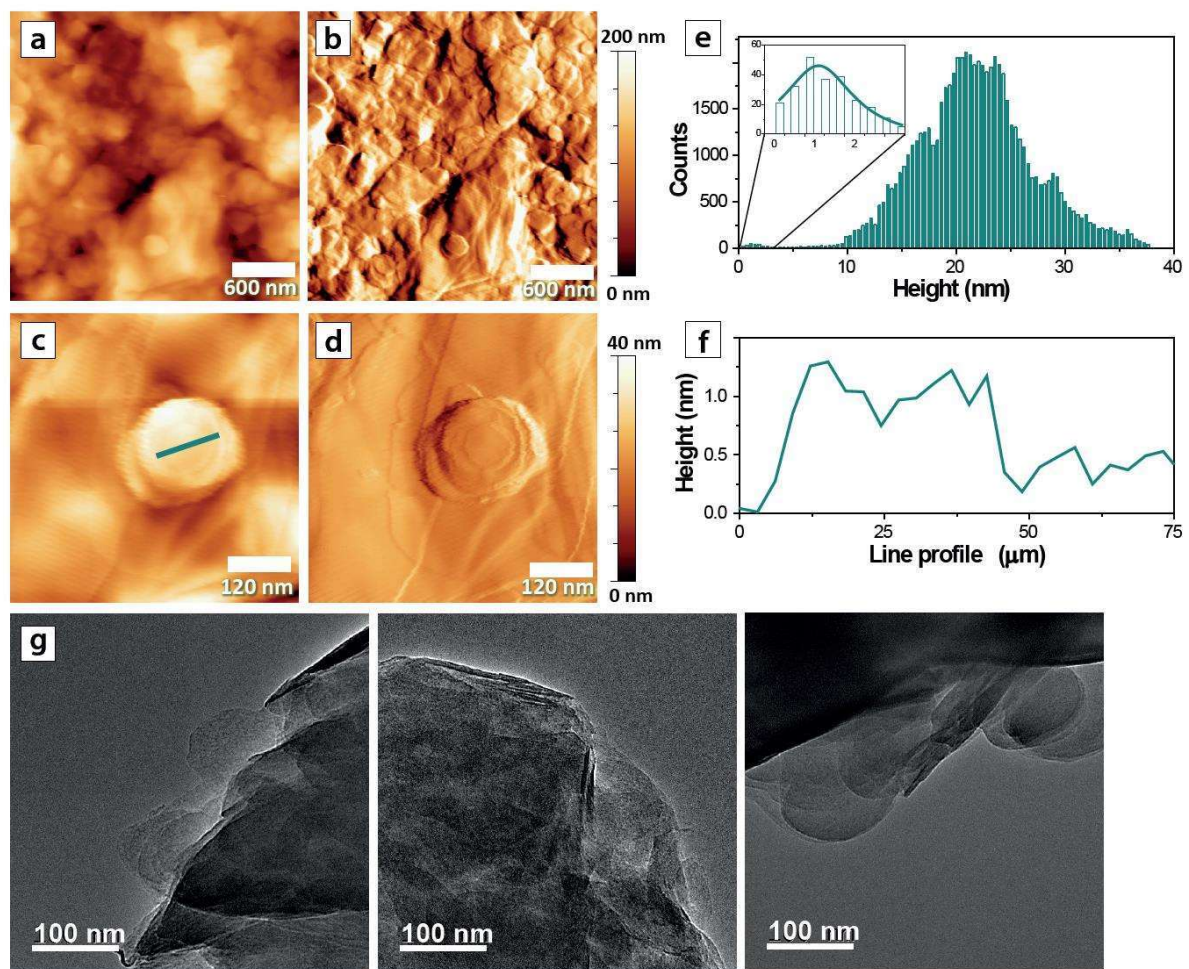
306  
307 **Fig. 2.** XRD patterns of Ni-saponites and *Gel\_Sap1.2* in comparison with *Sap1.2* (\* for capillary  
308 measurement): **(a)** Ni-saponites with modified interlayer space (*Sap1.2\_Ni-interl.* and *Sap1.2\_Ni-*  
309 *pillars*) at different relative humidities RH = 3, 10 and 80%; **(b)** Ni-saponites whose edges were modified  
310 (*Sap1.2\_Ni-edges1,2,3*) at RH = 80%; **(c)** the precursor gel (*Gel\_Sap1.2*).

### 311 3.2 AFM and TEM imaging

312 Figs. 3a-d show AFM images of a continuous film of *Sap1.2* deposited on a mica plate. Images  
313 acquired at a spatial scale from 3 to 0.6 μm and resolution around from 10 to 2.5 nm/px  
314 revealed the stacking of *Sap1.2* layers forming irregular shapes (Figs. 3c and 3d). The  
315 corresponding height histogram (Fig. 3e) shows the stacking of the saponite layers with an  
316 average height of 21.5 nm, in good agreement with the stacking length deduced from powder  
317 XRD measurements. Furthermore, the variations of about 1.35 nm observed at lower heights  
318 (see inset of Fig. 3e) are compatible with the d values deduced from XRD for smectite  
319 monolayers. This result agrees well with the height profile of Fig. 3f that corresponds to the

320 green line on Fig. 3c where height variations across a single TOT sheet can be observed. Such  
321 height variation reaches 1.1 - 1.2 nm as shown in Fig. 3c.  
322 The comparison of AFM and TEM images shows an almost hexagonal grain shape of the clay  
323 sheets for *Sap1.2* (Fig. 3g). Grain sizes are also consistent in between both techniques with an  
324 average grain size of 100 to 400 nm in diameter.

Figure 3



325  
326 **Fig. 3.** Topographical AFM images of *Sap1.2*: (a,c) height images and (b,d) deflection images of the  
327 saponite layers deposited on mica substrate. (e) Height histogram of Fig. 3c showing the size of the  
328 agglomerations and the inset showing the distribution for the smallest height. (f) Height profile

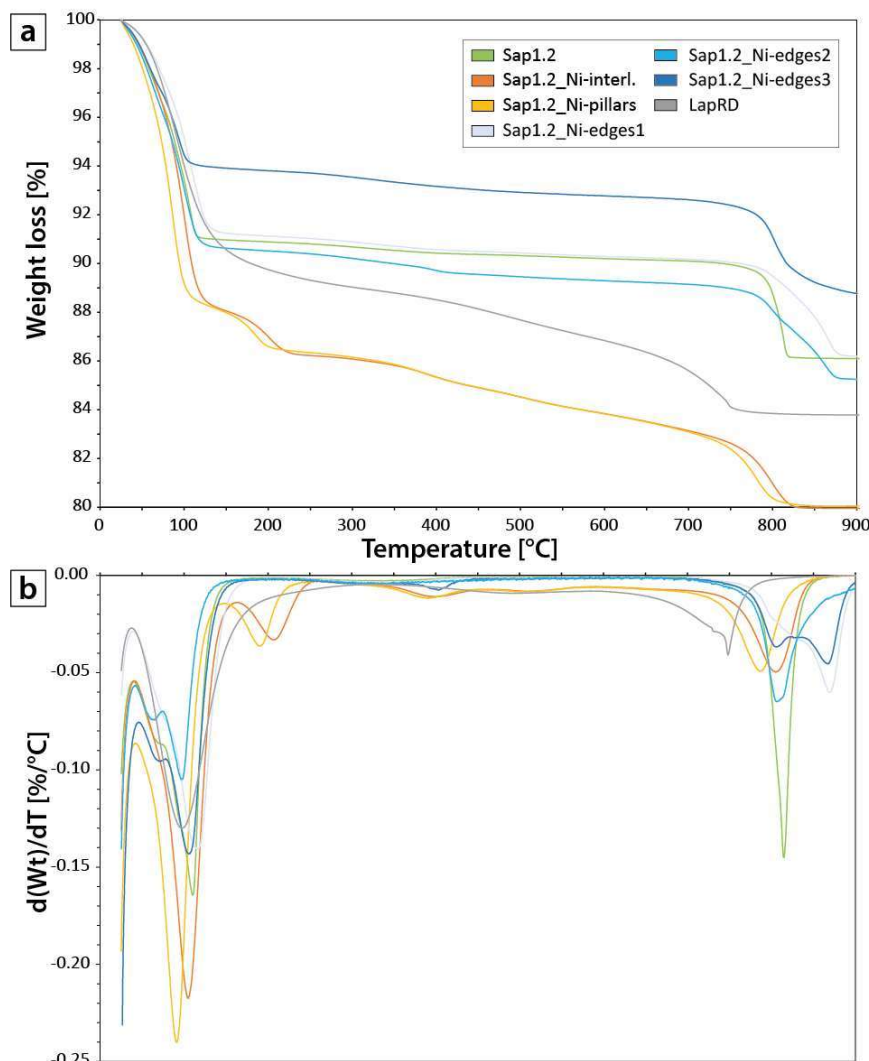
329 corresponding to the horizontal lines in the Fig. 3c which corresponds to the topography of a single  
330 (mainly rounded) saponite layer. (g) TEM images of *Sap1.2*.

### 331 **3.3 TGA results**

332 All samples (*LapRD*, *Sap1.2*, *Sap1.2\_Ni-interl.*, *Sap1.2\_Ni-pillars*, and *Sap1.2\_Ni-edges1,2,3*)  
333 show a major weight loss of 6 to 14% from ~ 100 °C up to ~ 250 °C (Fig. 4) corresponding to  
334 the removal of interlayer water. The overall amount of water release depends on the initial  
335 hydration state, which is imposed by the RH of the room atmosphere prior to the  
336 measurement. The *Sap1.2* on the one hand, and both the *Sap1.2\_Ni-interl.* and *Sap1.2\_Ni-*  
337 *pillars* on the other hand display different water loss at 150 °C: ~ 9 and 14 wt%, respectively.  
338 More water is attracted and retained by Ni<sup>2+</sup> and Ni(OH)<sub>2</sub> pillars than by Na<sup>+</sup> whose hydration  
339 energy is lower. However, as RH was not controlled, the overall amount of water release  
340 mainly depends on the initially lower hydration state of *Sap1.2* compared to the Ni-saponites.  
341 In addition, *Sap1.2\_Ni-interl.* and *Sap1.2\_Ni-pillars* display a second small weight loss of ~ 2%  
342 around 200 °C, and a third loss < 1% around ~ 400 °C. Such a phenomenon is only observed  
343 for samples with interlayer Ni. The small weight loss at 200 °C may correspond to the  
344 dehydration of remaining water linked to Ni<sup>2+</sup> or Ni(OH)<sub>2</sub> pillars. Indeed in the case of  
345 *Sap1.2\_Ni-interl.*, Ni<sup>2+</sup> cations have the ability to partly retain H<sub>2</sub>O molecules from its hydration  
346 sphere along dehydration [59,60]. The weight loss observed at 400 °C is well explained by the  
347 thermal decomposition of the Ni(OH)<sub>2</sub> pillars [61]. However, in the case of *Sap1.2\_Ni-interl.*,  
348 it is possible that water produced during the two firsts dehydration steps at 150 °C and 200  
349 °C, further reacts with Ni<sup>2+</sup> in the interlayers to form Ni(OH)<sub>2</sub> pillars during the TGA  
350 measurement. The dehydration of these latter pillars explaining the small weight loss  
351 observed at 400 °C for *Sap1.2\_Ni-interl.*. Finally, another major weight loss is also recorded

352 for all samples at temperature above 700 °C corresponding to the dehydroxylation process,  
1  
2  
3 353 i.e. the loss of OH groups from the structure, which is well-described for trioctahedral  
4  
5 354 smectites at these temperatures [62–64]. It can also be reported that *LapRD*, shows a slightly  
6  
7  
8 355 lower dehydroxylation temperature starting at ~ 700 °C. This shift likely results from the  
9  
10 356 smaller particle size of *LapRD* compared to saponite, thus improving the diffusion of water  
11  
12  
13 357 molecules [65].

Figure 4



358 **Fig. 4.** TGA and DTG profiles of Ni-saponites, *Sap1.2* and *LapRD*. Analysis were carried out from 25 °C  
359 to 900 °C at a ramp heating of 5 °C/min.

### 360 3.4 N<sub>2</sub> isotherms and textural characterization

361 Calculations of specific surface area give i) a  $S_{\text{BET}} = 31 \text{ m}^2/\text{g}$  for *Sap1.2*, ii) a range of  $S_{\text{BET}}$  from  
362 35 to  $40 \text{ m}^2/\text{g}$  for most of Ni-saponites, and iii) a  $S_{\text{BET}}$  of  $9 \text{ m}^2/\text{g}$  for *Sap1.2\_Ni-surface* (Table 1).  
363 The  $\text{N}_2$  isotherms of well-crystallized Ni-saponites are difficult to classify according to the  
364 IUPAC (International Union of Pure and Applied Chemistry) terminology (Fig. 5). On the one  
365 hand, their global shape present isotherms of type II, characteristic of non-porous materials  
366 [66]. The t-plot calculations also indicate the absence of microporosity (e.g. surface and  
367 volume of micropores close to zero). On the other hand, the presence of hysteresis loops  
368 typical for isotherms of type IV indicate capillary condensation effects occurring inside the  
369 pore space of the samples (Figs. 5a-d). Here, all saponites show hysteresis loops of H3/H4  
370 types from the IUPAC classification, typical of platy-shaped particles (H3) such as clay minerals  
371 [67]. The BJH, HK and DFT calculations were not applied on saponite, as the lack of  
372 conventional porosity from  $\text{N}_2$  isotherms, i.e. micro- or mesoporosity from the IUPAC  
373 classification, could lead to erroneous pore size distributions.

374  $\text{N}_2$  isotherm of *Gel\_Sap1.2* differs significantly from other well-crystallized saponite samples  
375 as it displays a clear shape of type I at low relative pressures, which indicates the presence of  
376 microporosity (i.e. pore size  $< 2 \text{ nm}$ ). It can be related to the intensity increase at small angle  
377 in XRD experiments. This is supported by t-plot calculations that give the following surface and  
378 a volume of microporosity:  $S_{\mu\text{pores}} = 77 \text{ m}^2/\text{g}$  and  $V_{\mu\text{pores}} = 0.029 \text{ cm}^3/\text{g}$ . The specific surface area  
379 calculation gives a  $S_{\text{BET}}$  of  $145 \text{ m}^2/\text{g}$ , which is up to 4 times higher than for its crystallized  
380 counterpart *Sap1.2*. Hysteresis loops also reveal capillary condensation in *Gel\_Sap1.2* porous  
381 structure.

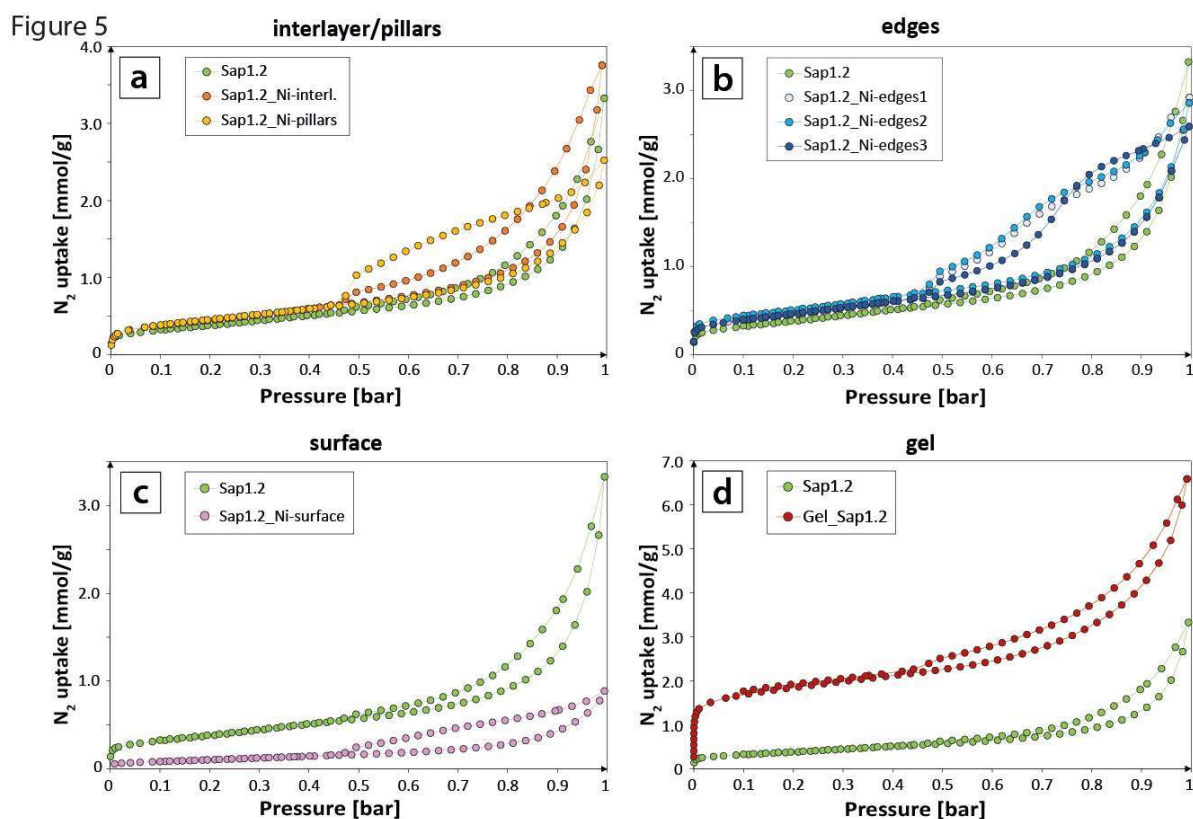


**Fig 5.** N<sub>2</sub> isotherms carried out at 1 bar and 77 K of *Sap1.2* compared to : (a) *Sap1.2\_Ni-interl.* and *Sap1.2\_Ni-pillars* ; (b) *Sap1.2\_Ni-edges1,2,3* ; (c) *Sap1.2\_Ni\_surface* ; and (d) *Gel\_Sap1.2*. All samples were outgassed at 150 °C prior to analysis.

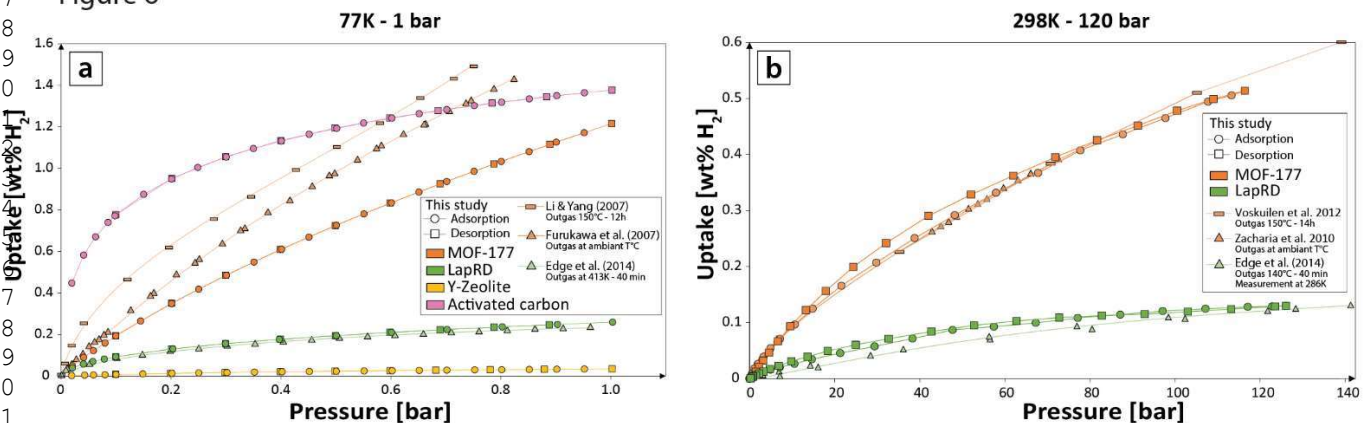
### 3.5 H<sub>2</sub> adsorption isotherms

#### 3.5.1 Assessment of H<sub>2</sub> adsorption procedures

Both low and high H<sub>2</sub> pressure isotherms were carried out on *MOF-177*, *Activated carbon*, *Y-zeolite* and *LapRD*, to compare H<sub>2</sub> uptakes with data from literature (Fig. 6; Table 1). At 77 K – 1 bar, the *Activated carbon* and *MOF-177* display the highest H<sub>2</sub> uptakes with 1.38 and 1.22 wt% H<sub>2</sub>, respectively (Fig. 6a). For *MOF-177*, our H<sub>2</sub> isotherm indicates a slightly lower uptake than that reported previously [44,45] at 77 K and around 0.8 bar (1.50 wt%). At high pressure (> 100 bar) and 298 K, the comparison of H<sub>2</sub> isotherms from this study and from the literature [17,31,46] for both *MOF-177* and *LapRD*, show a very good agreement with H<sub>2</sub> uptake of 0.12 and 0.50 wt% H<sub>2</sub> at 120 bar and 298 K for *LapRD* and *MOF-177*, respectively (Fig. 6b).

396 Specific surface areas were derived from N<sub>2</sub> isotherms and BET calculations. Our  
 397 measurements give a S<sub>BET</sub> of 3856 m<sup>2</sup>/g for *MOF-177*, consistent with values from literature  
 398 that range from 3100 to 4630 m<sup>2</sup>/g (see Table 1 and references therein). *Activated carbon* and  
 399 *Y-zeolite* show S<sub>BET</sub> of 872 and 677 m<sup>2</sup>/g, respectively, in good agreement with available data  
 400 [11,68]. *LapRD* has a S<sub>BET</sub> of 347 m<sup>2</sup>/g, which is consistent with the previous value from Edge  
 401 [17] of 399 m<sup>2</sup>/g calculated from DFT calculations on the same laponite (Table 1).  
 402 Slight bulk material density differences in-between these different studies may lead to minor  
 403 changes of the microporous networks. By way of consequence, S<sub>BET</sub> and H<sub>2</sub> uptake may slightly  
 404 vary from one preparation to other, as illustrated by the mechanically-densified *MOF-177*  
 405 from Zacharia et al. [46]. In addition, as outgassing conditions are not always identical from  
 406 one study to the other, direct comparison with data from literature may not be  
 407 straightforward. Whatever it is, the present benchmark exercise indicates a satisfactory  
 408 agreement between our data and those available in state-of-the-art studies under similar  
 409 operating conditions, thus validating the procedures used in the present work.

Figure 6

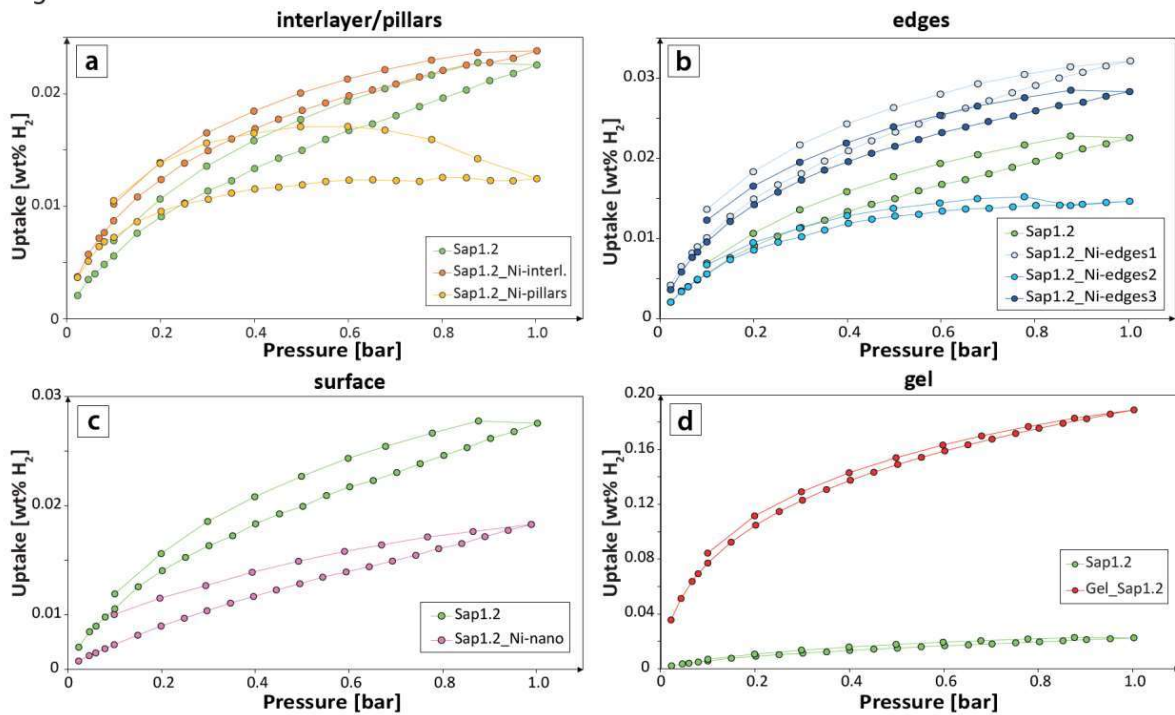


410 **Fig. 6.** H<sub>2</sub> isotherms of standards *MOF-177*, *LapRD*, *Y-zeolite* and *Activated carbon* from this study and  
 411 from the literature [17,31,44–46] carried out at : (a) 77 K and 1 bar ; and (b) at 298 K and 120 bar.  
 412 *LapRD* from Edge [17] is a Na-LaponiteRD similar to *LapRD* from this study.

### 3.5.2 H<sub>2</sub> isotherms of saponite and gel samples at 77 K - 1 bar

414 H<sub>2</sub> isotherms of saponites at 77 K – 1 bar show H<sub>2</sub> uptakes ranging from 0.01 to 0.03 wt% H<sub>2</sub>  
 415 for *Sap1.2\_Ni-pillars* and for *Sap1.2\_Ni-edges1*, respectively. These slight uptake differences  
 416 being within the uncertainty (around  $\pm 0.01$  wt% H<sub>2</sub> at 1 bar, calculated from *LapRD*  
 417 reproducibility measurements), no significant increase of H<sub>2</sub> uptake capacity could be  
 418 identified for Ni-saponites compared to *Sap1.2* whose H<sub>2</sub> uptake stands at 0.02 wt% (Figs. 7a-  
 419 c).  
 420 The precursor gel *Gel\_Sap1.2* is a significant exception with a maximum uptake of 0.19 wt%  
 421 H<sub>2</sub> at 1 bar H<sub>2</sub> pressure, which is by one order of magnitude higher than the capacity of *Sap1.2*  
 422 under the same conditions (Fig. 7d).

Figure 7

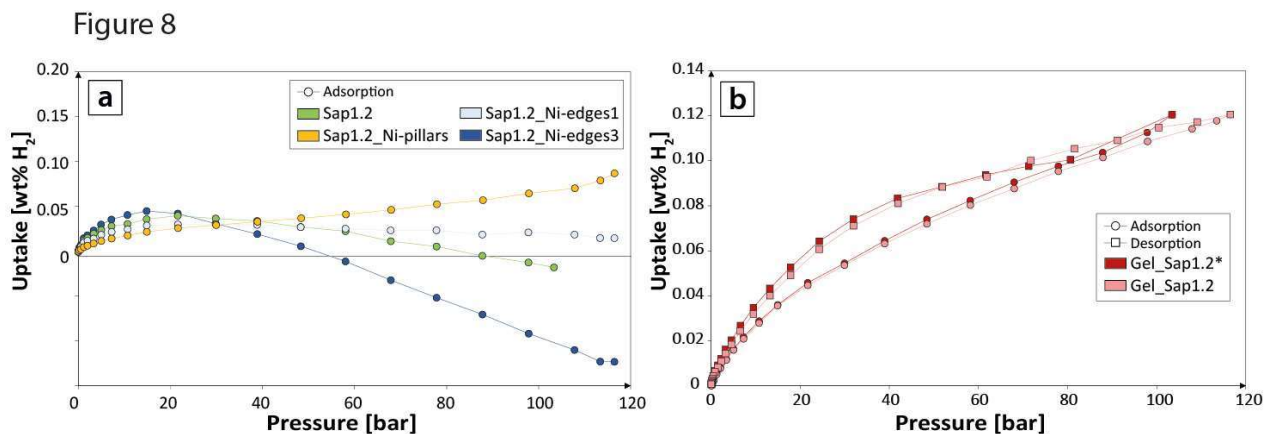


423  
 424 **Fig. 7.** H<sub>2</sub> isotherms carried out at 1 bar and 77 K of *Sap1.2* compared to : (a) *Sap1.2\_Ni-interl.* and  
 425 *Sap1.2\_Ni-pillars* ; (b) *Sap1.2\_Ni-edges1,2,3* ; (c) *Sap1.2\_Ni\_surface* ; and (d) *Gel\_Sap1.2*.

### 3.5.3 H<sub>2</sub> isotherms of saponite and gel samples at 298 K – 120 bar



427 H<sub>2</sub> isotherms acquisition at high pressure on these materials can be very challenging as the  
 428 following pitfalls must be overcome: (1) gas leakage due to the high diffusivity of H<sub>2</sub>, (2) a low  
 429 signal to noise ratio due to the low H<sub>2</sub> uptake capacity combined with low S<sub>BET</sub> of most saponite  
 430 samples, and (3) poorly-resolved volumetric due to the small mass of saponite (~ 250 mg) that  
 431 can be loaded in the ~ 200 mm<sup>3</sup> sample holder. Having in mind all these limitations, one can  
 432 conclude from Fig. 8a that H<sub>2</sub> uptake on saponites, with and without Ni<sup>2+</sup> in the structure, is  
 433 very low, remaining < 0.05 wt% for all saponite samples investigated.  
 434 Contrastingly, the precursor gel *Gel\_Sap1.2* shows a maximum H<sub>2</sub> uptake of 0.12 wt% H<sub>2</sub> at  
 435 120 bar and 298 K, and a very good reproducibility between the two replicate measurements  
 436 performed of the same sample (Fig. 8b).



437 **Fig 8.** H<sub>2</sub> isotherms carried out at 120 bar and 298 K on: (a) *Sap1.2*, *Sap1.2\_Ni-pillars*, *Sap1.2\_Ni-*  
 438 *edges1,3*; and (d) *Gel\_Sap1.2* and *Gel\_Sap1.2\** (replicate), whose isotherm was measured on the same  
 439 apparatus.  
 440

## 442 4. Discussion

### 443 4.1 Effect of porosity and Ni<sup>2+</sup> intercalation on H<sub>2</sub> adsorption on saponite 444 and nano-crystallized precursor at 1 bar – 77 K

445 At 1 bar and 77 K, all saponites show H<sub>2</sub> uptakes from 0.01 to 0.03 wt% H<sub>2</sub> and no clear  
1  
2  
3 446 tendency is highlighted in between Ni-saponites that could be assigned to a specific Ni  
4  
5 447 configuration in the structure. The *Gel\_sap1.2* shows a higher H<sub>2</sub> sorption capacity with a H<sub>2</sub>  
6  
7 448 uptake of 0.19 wt% H<sub>2</sub> at 1 bar - 77 K. Only few data from literature are available on smectite  
8  
9  
10 449 H<sub>2</sub> sorption capacities [25,69,70]. Gil et al. [25] recorded ~ 0.2 wt% H<sub>2</sub> at 1 bar and 77 K on an  
11  
12  
13 450 Al-pillared montmorillonite. These high uptakes are correlated with the presence of  
14  
15 451 microporosity whose volume (as determined by N<sub>2</sub> adsorption) reaches up to 0.080 cm<sup>3</sup>/g,  
16  
17  
18 452 which is well above values ~ 0.001 - 0.003 cm<sup>3</sup>/g determined for Ni-saponites in the present  
19  
20  
21 453 study (Table 1). The apparent hysteresis on saponite N<sub>2</sub> isotherms (Fig. 5) is likely produced by  
22  
23 454 inter-particles pore space, corresponding to a more complex porous network in comparison  
24  
25  
26 455 to conventional mesoporosity [71,72]. This is confirmed by the absence of a sorption plateau  
27  
28 456 at P/P<sub>0</sub> = 1. Here, the desorption curves of *Sap1.2\_Ni-pillars* and *Sap1.2\_Ni-edges1,2,3* display  
29  
30  
31 457 hysteresis loops larger than for *Sap1.2* and *Sap1.2\_Ni-interl.*, while having similar adsorption  
32  
33 458 branches (Fig. 5). As these samples cannot be considered as microporous, it is difficult to  
34  
35  
36 459 interpret these differences in term of pore geometries as classically commonly assumed [73].  
37  
38  
39 460 However it is likely that Ni<sup>2+</sup> and Ni(OH)<sub>2</sub> clusters/pillars affect *Sap1.2* structure in a sufficient  
40  
41 461 manner to impact capillary condensation during desorption by two main aspects: (1) the  
42  
43  
44 462 variation of hydration energy of smectite interlayer cation (*Sap1.2\_Ni-interl.*); and (2) the  
45  
46  
47 463 creation of “holes” in between pillars that may remain hydrated even at very low RH  
48  
49 464 conditions (*Sap1.2\_Ni-pillars*) as attested by the weight loss attributed to interlayer water  
50  
51  
52 465 removal above 150 °C (Fig. 4). In fact, intercalation of Ni<sup>2+</sup> in the saponite structure mainly  
53  
54 466 influences water retention as revealed by XRD and TGA data. Such effect is particularly visible  
55  
56  
57 467 for both the *Sap1.2\_Ni-interl.* and *Sap1.2\_Ni-pillars* (Figs. 2 and 4). However, there is no  
58  
59  
60  
61  
62  
63  
64  
65

1  
2  
3 468 increase of H<sub>2</sub> adsorption through the creation of Ni<sup>2+</sup>-bearing crystallographic sites compared  
4  
5  
6 469 to the Na-saturated *Sap1.2*.

7  
8  
9  
10  
11 470 Concerning the *Sap1.2\_Ni-surface* sample, the lower SSA may be explained according to Sarac  
12  
13  
14 471 Oztuna et al. [74]. The SSAs of functionalized porous subtract are slightly lower than that of  
15  
16 472 bare subtract because of pore clogging by nanoparticles. However, these authors have  
17  
18  
19 473 observed that the SSA gradually increased when Ni nanoparticles loading increases from 1.5  
20  
21 474 wt% to 20 wt%. Therefore, Ni amount may be optimized in order to minimize the SSA  
22  
23 475 reduction while providing the catalytic performances of metal loading.

24  
25  
26  
27 476 The *Gel\_sap1.2* is an exception as its micropores volume (0.029 cm<sup>3</sup>/g, as determined by N<sub>2</sub>  
28  
29  
30 477 adsorption) is much higher than the one of the well-crystallized saponites, but remains  
31  
32 478 relatively small for such a high H<sub>2</sub> uptake. This observation questions either the importance of  
33  
34 479 the textural control on H<sub>2</sub> adsorption or the relevance of N<sub>2</sub> adsorption results to characterize  
35  
36 480 the micropore volume available for H<sub>2</sub>, as discussed below.

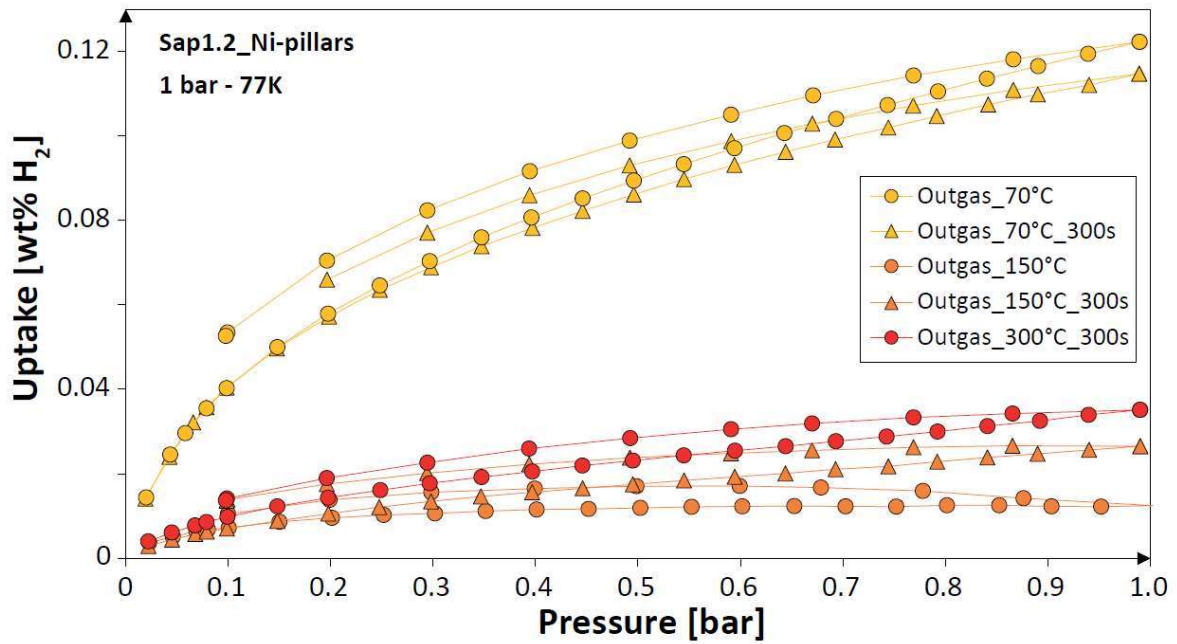
## 37 38 39 481 **4.2 Effect of outgassing condition**

40  
41  
42 482 Outgassing conditions, i.e. temperature and duration of the outgas prior to volumetric  
43  
44 483 measurements, have a strong impact on H<sub>2</sub> adsorption, as highlighted by Edge [17] study on  
45  
46 484 laponite who tested different degassing temperatures (from ambient temperature, and up to  
47  
48 485 160 °C under secondary vacuum condition) and observed very different H<sub>2</sub> uptakes (from 0.08  
49  
50 486 to 0.24 wt% H<sub>2</sub>). Ziemiański & Derkowski [29] also reveal that H<sub>2</sub> uptake on montmorillonite  
51  
52 487 significantly decreases with increasing outgassing temperature from 40 to 210 °C. Here,  
53  
54 488 sample outgassing at 70 °C, 150 °C, and 300 °C were carried out on *Sap1.2\_Ni-pillars* in order  
55  
56 489 to evaluate the effect of outgassing temperature on H<sub>2</sub> adsorption (Fig. 9). In particular, the  
57  
58 490 thermal treatment during outgassing impacts the hydration state inside the interlayer space.  
59  
60  
61  
62  
63  
64  
65

1  
2  
3  
4  
5  
6  
7  
8  
9  
10  
11  
12  
13  
14  
15  
16  
17  
18  
19  
20  
21  
22  
23  
24  
25  
26  
27  
28  
29  
30  
31  
32  
33  
34  
35  
36  
37  
38  
39  
40  
41  
42  
43  
44  
45  
46  
47  
48  
49  
50  
51  
52  
53  
54  
55  
56  
57  
58  
59  
60  
61  
62  
63  
64  
65

491 Here, a temperature outgas of 70 °C, instead of a routine 150 °C treatment, results in a  
492 significant sorption capacity increase from 0.05 wt% to 0.12 wt% H<sub>2</sub> at 77 K and 1 bar.  
493 Adsorption isotherms recorded after outgassing the sample at 150 °C or 300 °C are nearly  
494 identical. As previously observed from TGA results on this sample, dehydration is initiated at  
495 low RH and nearly fully completed at ~ 150 °C, and dehydroxylation of Ni(OH)<sub>2</sub> pillars occurs  
496 at ~ 400 °C. Then it is likely than sample outgassing at 150 °C or 300 °C lead to a partial or  
497 complete dehydration of *Sap1.2\_Ni-pillars* interlayer space, leading to its collapse despite the  
498 presence of pillars in between. Then such a collapse may prevent H<sub>2</sub> and N<sub>2</sub> to access these  
499 sorption sites. On the contrary, outgassing at 70 °C may allow the preservation of the pillars  
500 structure. In this case, the *d*<sub>001</sub>-spacing remains at about 14 Å. This value compares with 9.35  
501 Å in the uncharged anhydrous analogue, talc. Because of the Ni(OH)<sub>2</sub> pillars, the interlayer  
502 height of *Sap1.2\_Ni-pillars* is therefore  $d = (14 - 9.35) \text{ \AA} = 4.65 \text{ \AA}$ . This value is slightly higher  
503 than the kinetic diameter of H<sub>2</sub> (2.89 Å) and may be close to the optimum for H<sub>2</sub> to access the  
504 interlayer sorption sites [75]. These measurements nicely demonstrate the importance of the  
505 interlayer height for H<sub>2</sub> adsorption and the benefit of Ni(OH)<sub>2</sub> pillaring. We note that water  
506 hydration also allows to tune the interlayer height and may thus promote H<sub>2</sub> adsorption  
507 [23,29]. However, the outgassing step (heat and vacuum), that is a prerequisite before  
508 carrying out adsorption isotherms, may compromise a proper control of the hydration state  
509 of the samples as demonstrated by all our measurements performed after outgassing at 150  
510 °C (Fig. 7).

Figure 9 (Discussion)



511  
512 **Fig. 9.** H<sub>2</sub> isotherms at 1 bar and 77K of *Sap1.2\_Ni-pillars* at various outgassing and analysis conditions.  
513 Outgas temperatures of 70 °C, 150 °C, and 300 °C were tested, and equilibration time was increased  
514 to 300 s instead of 60 s.

515 In addition, a higher equilibration time (i.e. t = 300 s at each pressure increment instead of  
516 routine analysis t = 60 s, resulting in > 30 h of acquisition time for a complete isotherm) was  
517 also tested to evaluate H<sub>2</sub> adsorption kinetic. Indeed, H<sub>2</sub> diffusion to the adsorption site may  
518 also have to be accounted for the adsorption properties of the material. However, no positive  
519 effect related to the equilibration time was clearly recorded here on H<sub>2</sub> uptake.

### 520 **4.3 Effect of SSA influence on hydrogen adsorption capacity in porous** 521 **materials**

522 Several studies have already revealed the linear relationship between H<sub>2</sub> adsorption and the  
523 specific surface area at 1 bar and 77 K on different types of porous materials [30,76,77]. Such

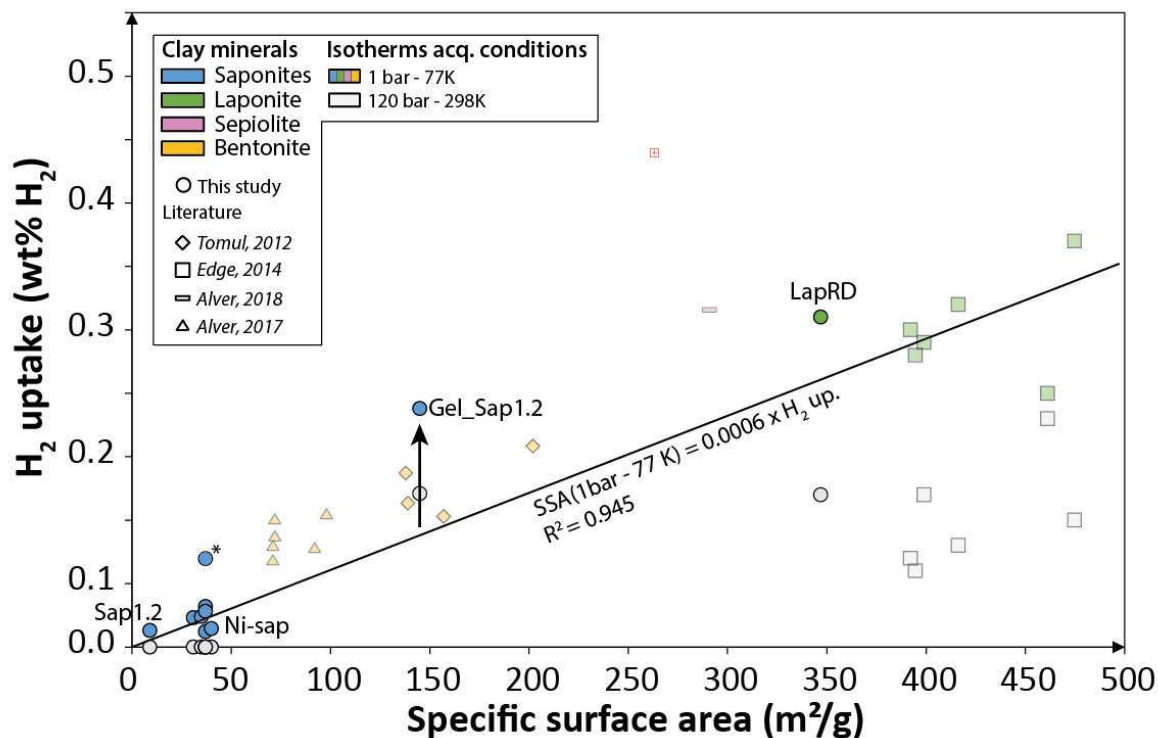
1  
2  
3 524 a trend is also observed here (Fig. 10, colourful symbols), up to almost 500 m<sup>2</sup>/g for the upper  
4  
5 525 SSA range corresponding to laponite.

6  
7 526 It is quite clear that samples having a high SSA, also display a high microporosity. In the case  
8  
9 527 of both *LapRD* or *Gel\_Sap1.2* the  $S_{\mu\text{pore}}$  (340 m<sup>2</sup>/g and 77 m<sup>2</sup>/g) stand for ~ 98% and ~ 50% of  
10  
11 528  $S_{\text{BET}}$  (347 m<sup>2</sup>/g and 145 m<sup>2</sup>/g), respectively (Table 1). Such a conclusion has also been reached  
12  
13 529 previously [31] for MOFs and activated carbons. Therefore, it is likely that micropores are  
14  
15 530 responsible for much of the H<sub>2</sub> adsorption capacity. This observation makes sense when  
16  
17 531 considering that a good match in-between micropores and H<sub>2</sub> kinetic diameter (2.89 Å) is a  
18  
19 532 prerequisite for enhanced H<sub>2</sub> adsorption.

20  
21  
22  
23  
24 533 We also point out that N<sub>2</sub> BET measurements do not allow probing the interlayer space. Thus,  
25  
26  
27 534 it is coherent that clay samples whose interlayer space has collapsed because of outgassing at  
28  
29 535 150 °C are all plotted along this linear correlation in between H<sub>2</sub> adsorption and the specific  
30  
31  
32 536 surface. It also explains why *Sap1.2\_Ni-pillars* outgassed at 70 °C, whose interlayer is still  
33  
34  
35 537 accessible to H<sub>2</sub>, plots well above this line.

36  
37  
38  
39  
40  
41  
42  
43  
44  
45  
46  
47  
48  
49  
50  
51  
52  
53  
54  
55  
56  
57  
58  
59  
60  
61  
62  
63  
64  
65

Figure 10



538  
539 **Fig. 10.** H<sub>2</sub> uptakes of clay minerals from this study and the literature at 1 bar - 77 K and 120 bar – 298  
540 K. The linear trend correlating SSA and H<sub>2</sub> uptake was calculated at 1 bar - 77 K for saponite and  
541 laponite. \*: *Sap1.2\_Ni-pillars* with temperature outgas of 70 °C.

#### 542 **4.4 Performance of saponite and related gel at 120 bar – 298 K**

543 All saponites show H<sub>2</sub> uptakes < 0.05 wt% at 120 bar and 298 K, and the *Gel\_sap1.2* shows a  
544 higher H<sub>2</sub> sorption capacity of 0.12 wt% H<sub>2</sub>. At ambient temperature and above, Mondelli et  
545 al. [69] and Bardelli et al. [70] recorded H<sub>2</sub> sorption capacities of ~ 0.20 and 0.25 wt% H<sub>2</sub> at 90  
546 °C and 80 bar H<sub>2</sub> pressure on Na-montmorillonite and purified clay fraction (mainly illite-  
547 smectite) of a Callovo-Oxfordian claystone, respectively. However, these values are intriguing  
548 for two reasons. First, they are very high regarding both the elevated temperature condition  
549 and the low specific surface area of these materials (< 40 m<sup>2</sup>/g). Second, they slightly increase  
550 with temperature from 28 to 90 °C [70], which is not thermodynamically consistent. Recently,

1  
2  
3 552 130 m<sup>2</sup>/g does not exceed 0.02 wt% at 298 K and 145 bar. They also confirmed that this H<sub>2</sub>  
4  
5 553 uptake logically decreases significantly with temperature increase.

6  
7  
8 554 The linear relationship in between S<sub>BET</sub> (as measured by N<sub>2</sub> adsorption) and H<sub>2</sub> uptake does  
9  
10  
11 555 not seem to be valid at high pressure and ambient temperature (Fig. 10, grey symbols). H<sub>2</sub>  
12  
13 556 sorption capacities drastically decrease as temperature increases, and that pressure increase  
14  
15  
16 557 does not compensate for this decrease. In the case of saponite, H<sub>2</sub> uptake is below 0.05 wt%  
17  
18 558 H<sub>2</sub> at 298 K and 100 bar. Clay-related materials with higher S<sub>BET</sub>, like *Gel\_Sap1.2* and laponites  
19  
20  
21 559 (*LapRD*; [17]), do adsorb modest amount of H<sub>2</sub> under such conditions (> 0.2 wt%), but SSA in  
22  
23  
24 560 itself is not sufficient to predict their H<sub>2</sub> adsorption capacity. For example, the *Gel\_Sap1.2*  
25  
26 561 shows similar H<sub>2</sub> uptake at 120 bar and 298 K than laponites despite contrasting SSA values  
27  
28  
29 562 (SSA = 145 and 392 - 475 m<sup>2</sup>/g, respectively). Thus, the SSA and micropore volume determined  
30  
31  
32 563 by N<sub>2</sub> adsorption does not seem to be relevant to characterize the properties of the materials  
33  
34 564 with respect to H<sub>2</sub> adsorption, at least at high pressure and ambient temperature. Ziemiański  
35  
36  
37 565 & Derkowski [29] clearly reveal that micropore volume determined by CO<sub>2</sub>, a molecule that  
38  
39  
40 566 display a kinetic diameter closer to H<sub>2</sub> (2.89 and 3.3 Å for H<sub>2</sub> and CO<sub>2</sub> respectively), is much  
41  
42 567 more appropriate.

#### 45 568 **4.5 Gels of clays: new perspectives for H<sub>2</sub> sorption ?**

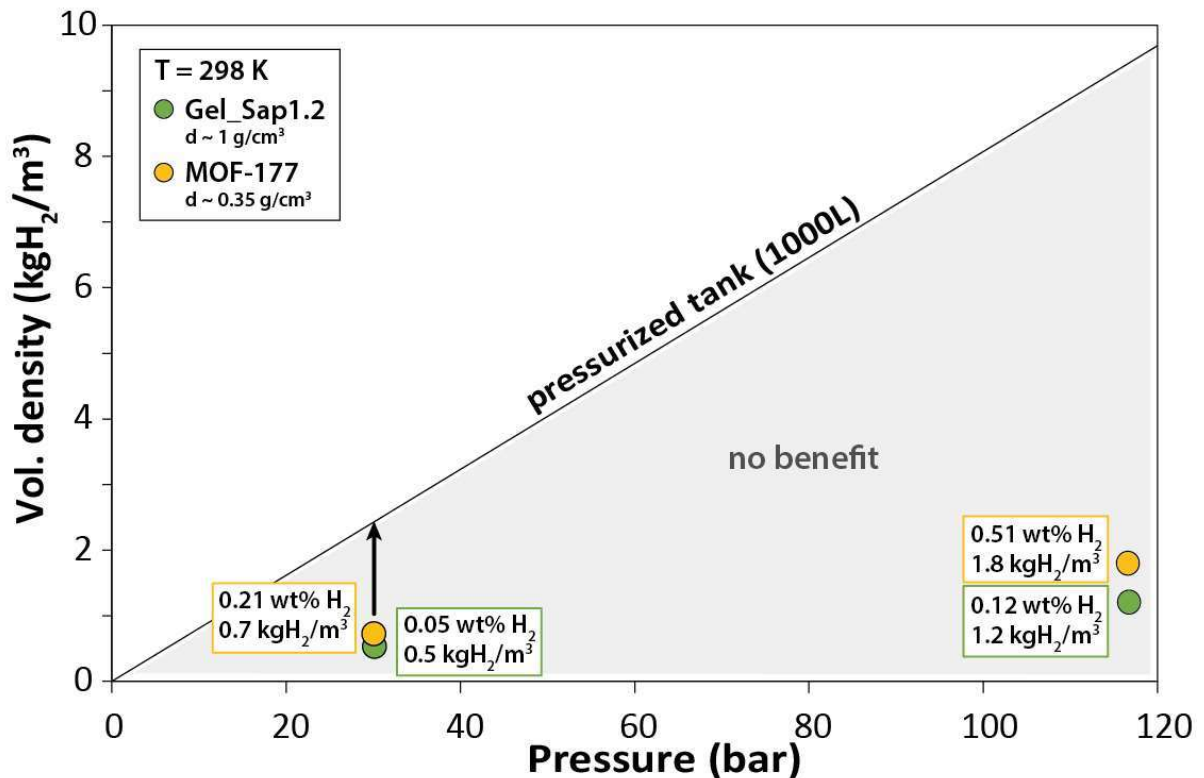
46  
47  
48  
49 569 The emphasis for much research on H<sub>2</sub> storage has been placed in the limiting requirements  
50  
51 570 for mobile applications, hitherto excluding clays because of their intrinsic weight. But large-  
52  
53  
54 571 scale storages do not bear the same constraints. In this context, clay minerals have several  
55  
56  
57 572 very attractive properties such as large surface area, low cost, and environmental safety.  
58  
59 573 Representing volumetric density (i.e. kgH<sub>2</sub>/m<sup>3</sup>) instead of gravimetric density (i.e. wt% H<sub>2</sub>) is  
60  
61  
62  
63  
64  
65



574 particularly relevant when comparing different materials, as their mass densities may be very  
1  
2  
3 575 different. Fig. 11 compares H<sub>2</sub> storage capacities at 298 K, a temperature of interest for large  
4  
5 576 scale storage, for both *Gel\_Sap1.2* and the well-studied *MOF-177*, at two different pressure:  
6  
7  
8 577 30 and 120 bar. First, by strictly comparing their volumetric density, i.e. their mass capacity  
9  
10 578 for storing H<sub>2</sub> in a given volume (here 1 m<sup>3</sup>), *Gel\_Sap1.2* shows a comparable performance  
11  
12  
13 579 with *MOF-177*. In particular, at 30 bar and 298 K both materials have nearly identical H<sub>2</sub>  
14  
15 580 volumetric densities of 0.5 kgH<sub>2</sub>/m<sup>3</sup>. Ambient temperature associated with a few tens of bars  
16  
17  
18 581 being ideal conditions for an industrial application, like a stationary underground H<sub>2</sub> storage,  
19  
20  
21 582 it is thus interesting to notice the high potential of *Gel\_Sap1.2*.  
22  
23  
24 583 Even if MOFs, as well as *Gel\_Sap1.2*, do not display sufficient H<sub>2</sub> uptake to make them useful  
25  
26  
27 584 for H<sub>2</sub> storage at ambient temperature, one may notice that a low cost and easy-to-produce  
28  
29 585 material like gel performs as well as very expensive MOFs. Thus, this gel of clay material is a  
30  
31  
32 586 new and promising porous material. Its sorption capacities may be enhanced by compaction  
33  
34 587 (increase the volumetric density) and by acid treatment, as classically used for enhancing  
35  
36  
37 588 specific surface area [27].  
38  
39  
40 589 Up to now, all the research effort on H<sub>2</sub> physisorption has focused on crystallized nano-  
41  
42  
43 590 materials (e.g. MOFs, zeolites, carbon nano-fibers) whose pore size is dimensioned to  
44  
45 591 approach the kinetic diameter of the H<sub>2</sub> molecule. The alumino-silicate gel displays sorption  
46  
47  
48 592 capacities that are 2 to 5 times higher than their crystalline equivalent, even at ambient  
49  
50  
51 593 temperature. By definition, the so call *Gel\_Sap1.2* is supposed to be amorphous, but XRD  
52  
53 594 patterns (Fig. 2c) attest for the presence of small or poorly crystalline phases. In addition, it  
54  
55  
56 595 displays high specific surface area (~ 150 m<sup>2</sup>/g) and high micropore volumes ( $V_{\mu\text{pores}} = 0.029$   
57  
58 596 cm<sup>3</sup>/g). This “gel” is therefore the antithesis of all crystallized substrates studied so far. A  
59  
60  
61  
62  
63  
64  
65

597 specific point to further investigate to better understand the global structure of this material  
598 and more specifically the localization of micropores. Its ambient sorption properties are still  
599 too low to justify a stationary storage application, but an improvement in its capacity by a  
600 factor of 2 would already allow a significant gain compared to classical pressurized storage.

Figure 11



601  
602 **Fig. 11.** Hydrogen volumetric densities of *Gel\_Sap1.2* at 30 bar and 120 bar compared to *MOF-177* at  
603 ambient temperature. The black arrow indicates the density objective to reach to have an economic  
604 interest in storing H<sub>2</sub> physisorbed inside clays instead of gaseous storing in pressurized tank.

## 606 5. Conclusion

607 N<sub>2</sub> and H<sub>2</sub> isotherms measurements performed at 77 K – 1 bar and 298 K – 120 bar on *Sap1.2*  
608 and Ni-saponites record low SSAs ranging from 9 to 40 m<sup>2</sup>/g and modest H<sub>2</sub> uptakes of ~ 0.03

609 wt% H<sub>2</sub> at 77 K – 1 bar, and < 0.05 wt% H<sub>2</sub> at 298 K – 120 bar. These low values indicate that  
610 Ni functionalization do not create specific crystallographic sites for H<sub>2</sub> adsorption. However, it  
611 is observed that H<sub>2</sub> uptake is strongly controlled by external conditions, in particular  
612 outgassing temperature that influences the interlayer space opening through its hydration  
613 state. Measurements on Ni-pillared saponite highlight that an outgas of 70 °C preserves the  
614 interlayer space porosity for H<sub>2</sub> adsorption, in comparison to other saponites routinely  
615 outgassed at 150 °C. It is likely that H<sub>2</sub> can only access the inter particles pore space and the  
616 basal and lateral adsorption sites in these latter samples outgassed at 150 °C. This is supported  
617 by the linear correlation in between SSA and H<sub>2</sub> uptake at 1 bar and 77 K, illustrating that  
618 neither N<sub>2</sub> nor H<sub>2</sub> enter porosity inside the structure.

619 The precursor gel (*Gel\_Sap1.2*) used for saponite synthesis, is an exception as it displays an  
620 SSA of 145 m<sup>2</sup>/g together with a high microporosity and an H<sub>2</sub> uptake of 0.19 wt% at 77 K and  
621 1 bar, and up to 0.12 wt% at 298 K and 120 bar. This latter uptake is equivalent to what can  
622 achieve the *MOF-177* under identical conditions. Further investigations on precursor gel  
623 materials are needed for their microporous features and good potential for high H<sub>2</sub> uptakes.

624

## 625 **Acknowledgements**

626 This work was financially supported by ORANO industry and the ANR OCCAMH2. The  
627 geochemistry-mineralogy platform of ISTERre (Grenoble, France) used for most measurements  
628 is partially funded by a grant from Labex OSUG@2020 (investissements d'avenir, ANR10-  
629 LABX56").

630

## 631 References

- 1  
2  
3  
4 632 [1] Jain IP, Lal C, Jain A. Hydrogen storage in Mg: A most promising material. *Int J*  
5  
6 633 *Hydrogen Energy* 2010;35:5133–44. <https://doi.org/10.1016/j.ijhydene.2009.08.088>.  
7  
8 634 [2] Ren J, Musyoka NM, Langmi HW, Mathe M, Liao S. Current research trends and  
9  
10 635 perspectives on materials-based hydrogen storage solutions: A critical review. *Int J*  
11  
12 636 *Hydrogen Energy* 2017;42:289–311. <https://doi.org/10.1016/j.ijhydene.2016.11.195>.  
13  
14  
15 637 [3] Barthelemy H, Weber M, Barbier F. Hydrogen storage: Recent improvements and  
16  
17 638 industrial perspectives. *Int J Hydrogen Energy* 2017;42:7254–62.  
18  
19 639 <https://doi.org/10.1016/j.ijhydene.2016.03.178>.  
20  
21 640 [4] Kaye SS, Dailly A, Yaghi OM, Long JR. Impact of preparation and handling on the  
22  
23 641 hydrogen storage properties of Zn<sub>4</sub>O(1,4-benzenedicarboxylate)<sub>3</sub> (MOF-5). *J Am*  
24  
25 642 *Chem Soc* 2007;129:14176–7. <https://doi.org/10.1021/ja076877g>.  
26  
27  
28 643 [5] Han D, Jiang FL, Wu MY, Chen L, Chen QH, Hong MC. A non-interpenetrated porous  
29  
30 644 metal-organic framework with high gas-uptake capacity. *Chem Commun*  
31  
32 645 2011;47:9861–3. <https://doi.org/10.1039/c1cc12858b>.  
33  
34  
35 646 [6] Langmi HW, Walton A, Al-Mamouri MM, Johnson SR, Book D, Speight JD, et al.  
36  
37 647 Hydrogen adsorption in zeolites A, X, Y and RHO. *J Alloys Compd* 2003;356–357:710–  
38  
39 648 5. [https://doi.org/10.1016/S0925-8388\(03\)00368-2](https://doi.org/10.1016/S0925-8388(03)00368-2).  
40  
41 649 [7] Langmi HW, Ren J, North B, Mathe M, Bessarabov D. Hydrogen storage in metal-  
42  
43 650 organic frameworks: A review. *Electrochim Acta* 2014;128:368–92.  
44  
45 651 <https://doi.org/10.1016/j.electacta.2013.10.190>.  
46  
47  
48 652 [8] Ramirez-Cuesta AJ, Mitchell PCH. Hydrogen adsorption in a copper ZSM5 zeolite. An  
49  
50 653 inelastic neutron scattering study. *Catal Today* 2007;120:368–73.  
51  
52 654 <https://doi.org/10.1016/j.cattod.2006.09.024>.  
53  
54  
55 655 [9] Kadono K, Kajiura H, Shiraishi M. Dense hydrogen adsorption on carbon subnanopores  
56  
57 656 at 77 K. *Appl Phys Lett* 2003;83:3392–4. <https://doi.org/10.1063/1.1621073>.  
58  
59 657 [10] Patchkovskii S, Tse JS, Yurchenko SN, Zhechkov L, Heine T, Seifert G. Graphene  
60  
61  
62  
63  
64  
65

- 658 nanostructures as tunable storage media for molecular hydrogen. Proc Natl Acad Sci U  
659 S A 2005;102:10439–44. <https://doi.org/10.1073/pnas.0501030102>.
- 660 [11] Jordá-Beneyto M, Suárez-García F, Lozano-Castelló D, Cazorla-Amorós D, Linares-  
661 Solano A. Hydrogen storage on chemically activated carbons and carbon  
662 nanomaterials at high pressures. Carbon N Y 2007;45:293–303.  
663 <https://doi.org/10.1016/j.carbon.2006.09.022>.
- 664 [12] DeSantis D, Mason JA, James BD, Houchins C, Long JR, Veenstra M. Techno-economic  
665 Analysis of Metal-Organic Frameworks for Hydrogen and Natural Gas Storage. Energy  
666 and Fuels 2017;31:2024–32. <https://doi.org/10.1021/acs.energyfuels.6b02510>.
- 667 [13] Li J, Corma A, Yu J. Synthesis of new zeolite structure. Chem Soc Rev 2013;44:7112–  
668 27. <https://doi.org/10.1039/x0xx00000x>.
- 669 [14] Ding M, Cai X, Jiang HL. Improving MOF stability: Approaches and applications. Chem  
670 Sci 2019;10:10209–30. <https://doi.org/10.1039/c9sc03916c>.
- 671 [15] Kumar P, Anand B, Tsang YF, Kim KH, Khullar S, Wang B. Regeneration, degradation,  
672 and toxicity effect of MOFs: Opportunities and challenges. Environ Res  
673 2019;176:108488. <https://doi.org/10.1016/j.envres.2019.05.019>.
- 674 [16] Bhatia SK, Myers AL. Optimum conditions for adsorptive storage. Langmuir  
675 2006;22:1688–700. <https://doi.org/10.1021/la0523816>.
- 676 [17] Edge J. Hydrogen adsorption and dynamics in clay minerals. 2014.
- 677 [18] Neumann BS, Sansom KG. The formation of stable sols from laponite, a synthetic  
678 hectorite-like clay. Clay Miner 1970;8:389–404.
- 679 [19] Cool P, Vansant EF. Preparation and characterization of zirconium pillared laponite  
680 and hectorite. Microporous Mater 1996;6:27–36. [https://doi.org/10.1016/0927-  
681 6513\(95\)00080-1](https://doi.org/10.1016/0927-6513(95)00080-1).
- 682 [20] Schaeff HT, Loring JS, Glezakou V-A, Miller QRS, Chen J, Owen AT, et al. Competitive  
683 sorption of CO<sub>2</sub> and H<sub>2</sub>O in 2:1 layer phyllosilicates. Geochim Cosmochim Acta  
684 2015;161:248–57. <https://doi.org/10.1051/0004-6361/202038870>.
- 685 [21] Yang N, Liu S, Yang X. Molecular simulation of preferential adsorption of CO<sub>2</sub> over CH<sub>4</sub>

- 686 in Na-montmorillonite clay material. Appl Surf Sci 2015;356:1262–71.  
687 <https://doi.org/10.1016/j.apsusc.2015.08.101>.
- 688 [22] Busch A, Bertier P, Gensterblum Y, Rother G, Spiers CJ, Zhang M, et al. On sorption  
689 and swelling of CO<sub>2</sub> in clays. Geomech Geophys Geo-Energy Geo-Resources  
690 2016;2:111–30. <https://doi.org/10.1007/s40948-016-0024-4>.
- 691 [23] Grekov DI, Suzuki-Muresan T, Kalinichev AG, Pré P, Grambow B. Thermodynamic data  
692 of adsorption reveal the entry of CH<sub>4</sub> and CO<sub>2</sub> in smectite clay interlayer. Phys Chem  
693 Chem Phys 2020;19. <https://doi.org/10.1039/D0CP02135K>.
- 694 [24] Ziemiański PP, Derkowski A, Szczurowski J, Kozieł M. The structural versus textural  
695 control on the methane sorption capacity of clay minerals. Int J Coal Geol 2020;224.  
696 <https://doi.org/10.1016/j.coal.2020.103483>.
- 697 [25] Gil A, Trujillano R, Vicente MA, Korili SA. Hydrogen adsorption by microporous  
698 materials based on alumina-pillared clays. Int J Hydrogen Energy 2009;34:8611–5.  
699 <https://doi.org/10.1016/j.ijhydene.2009.08.057>.
- 700 [26] Erdoğan Alver B. Adsorption studies of hydrogen and ethylene on cation-exchanged  
701 bentonite. Clay Miner 2017;52:67–73.  
702 <https://doi.org/10.1180/claymin.2017.052.1.04>.
- 703 [27] Erdoğan Alver B. Hydrogen adsorption on natural and sulphuric acid treated sepiolite  
704 and bentonite. Int J Hydrogen Energy 2018;43:831–8.  
705 <https://doi.org/10.1016/j.ijhydene.2017.10.159>.
- 706 [28] Edge JS, Skipper NT, Fernandez-alonso F, Lovell A, Srinivas G, Bennington SM, et al.  
707 Structure and Dynamics of Molecular Hydrogen in the Interlayer Pores of a Swelling  
708 2:1 Clay by Neutron Scattering. J Phys Chem 2014;118:25740–7.  
709 <https://doi.org/10.1021/jp5082356>.
- 710 [29] Ziemiański PP, Derkowski A. Structural and textural control of high-pressure hydrogen  
711 adsorption on expandable and non- expandable clay minerals in geologic conditions.  
712 Int J Hydrogen Energy 2022. <https://doi.org/10.1016/j.ijhydene.2022.06.204>.
- 713 [30] Thomas KM. Adsorption and desorption of hydrogen on metal-organic framework

- 714 materials for storage applications: Comparison with other nanoporous materials. *Dalt*  
715 *Trans* 2009;1487–505. <https://doi.org/10.1039/b815583f>.
- 716 [31] Voskuilen TG, Pourpoint TL, Dailly AM. Hydrogen adsorption on microporous materials  
717 at ambient temperatures and pressures up to 50 MPa. *Adsorption* 2012;18:239–49.  
718 <https://doi.org/10.1007/s10450-012-9397-z>.
- 719 [32] Ray SS, Okamoto K, Okamoto M. Structure - Property Relationship in Biodegradable  
720 Poly(butylene succinate )/Layered Silicate Nanocomposites. *Macromolecules*  
721 2003;2355–67. <https://doi.org/10.1021/ma021728y>.
- 722 [33] Claverie M, Garcia J, Prevost T, Brendlé J, Limousy L. Inorganic and hybrid (organic-  
723 inorganic) lamellar materials for heavy metals and radionuclides capture in energy  
724 wastes management-A review. *Materials (Basel)* 2019;12:1–25.  
725 <https://doi.org/10.3390/ma12091399>.
- 726 [34] Zhou CH, Zhou Q, Wu QQ, Petit S, Jiang XC, Xia ST, et al. Modification, hybridization  
727 and applications of saponite: An overview. *Appl Clay Sci* 2019;168:136–54.  
728 <https://doi.org/10.1016/j.clay.2018.11.002>.
- 729 [35] Bergaoui L, Lambert JF, Vicente-Rodriguez MA, Michot LJ, Villieras F. Porosity of  
730 synthetic saponites with variable layer charge pillared by Al<sup>13</sup> polycations. *Langmuir*  
731 1995;11:84–7. <https://doi.org/10.1021/la00008a001>.
- 732 [36] Molinard A, Vansant EF. Controlled gas adsorption properties of various pillared clays.  
733 *Adsorption* 1995;1:49–59. <https://doi.org/10.1007/BF00704145>.
- 734 [37] Kloprogge T. Synthesis of smectites and porous pillared clay catalysts: a review. *J*  
735 *Porous Mater* 1998;5:5–41. <https://doi.org/10.1023/A>.
- 736 [38] Wang K, Yan X, Komarneni S. CO<sub>2</sub> Adsorption by Several Types of Pillared  
737 Montmorillonite Clays. *Appl Petrochemical Res* 2018;8:173–7.  
738 <https://doi.org/10.1007/s13203-018-0206-9>.
- 739 [39] Carraro P, Elías V, Blanco AG, Sapag K, Moreno S, Oliva M, et al. Synthesis and multi-  
740 technique characterization of nickel loaded MCM-41 as potential hydrogen-storage  
741 materials. *Microporous Mesoporous Mater* 2014;191:103–11.

- 742 <https://doi.org/10.1016/j.micromeso.2014.03.005>.
- 1  
2  
3 743 [40] Carraro PM, Blanco AAG, Soria FA, Lener G, Sapag K, Eimer GA, et al. Understanding  
4 744 the role of nickel on the hydrogen storage capacity of Ni / MCM-41 materials.  
5  
6 745 Microporous Mesoporous Mater 2016;231:31–9.  
7  
8 746 <https://doi.org/10.1016/j.micromeso.2016.05.017>.
- 9  
10  
11 747 [41] Forster PM, Eckert J, Heiken BD, Parise JB, Yoon JW, Jhung SH, et al. Adsorption of  
12  
13 748 molecular hydrogen on coordinatively unsaturated Ni(II) sites in a nanoporous hybrid  
14  
15 749 material. J Am Chem Soc 2006;128:16846–50. <https://doi.org/10.1021/ja0649217>.
- 16  
17 750 [42] Brindley GW, Bish DL, Wan H-M. Compositions, structures, and properties of nickel-  
18  
19 751 containing minerals in the kerolite-pimelite series. Am Mineral 1979;64:615–625.
- 20  
21  
22 752 [43] Manceau A, Calas G. Heterogeneous distribution of nickel in hydrous silicates from  
23  
24 753 New Caledonia ore deposits. Am Mineral 1985;70:549–58.
- 25  
26 754 [44] Furukawa H, Miller MA, Yaghi OM. Independent verification of the saturation  
27  
28 755 hydrogen uptake in MOF-177 and establishment of a benchmark for hydrogen  
29  
30 756 adsorption in metal-organic frameworks. J Mater Chem 2007;17:3197–204.  
31  
32 757 <https://doi.org/10.1039/b703608f>.
- 33  
34  
35 758 [45] Li Y, Yang RT. Gas adsorption and storage in metal-organic framework MOF-177.  
36  
37 759 Langmuir 2007;23:12937–44. <https://doi.org/10.1021/la702466d>.
- 38  
39  
40 760 [46] Zacharia R, Cossement D, Lafi L, Chahine R. Volumetric hydrogen sorption capacity of  
41  
42 761 monoliths prepared by mechanical densification of MOF-177. J Mater Chem  
43  
44 762 2010;20:2145–51. <https://doi.org/10.1039/b922991d>.
- 45  
46 763 [47] Anthony JW, Bideaux RA, Bladh KW, Nichols MC. Handbook of Mineralogy. 2001.
- 47  
48  
49 764 [48] Schlegel ML, Manceau A, Charlet L, Chateigner D, Hazemann JL. Sorption of metal ions  
50  
51 765 on clay minerals. III. Nucleation and epitaxial growth of Zn phyllosilicate on the edges  
52  
53 766 of hectorite. Geochim Cosmochim Acta 2001;65:4155–70.  
54  
55 767 [https://doi.org/10.1016/S0016-7037\(01\)00700-1](https://doi.org/10.1016/S0016-7037(01)00700-1).
- 56  
57 768 [49] Dähn R, Scheidegger AM, Manceau A, Schlegel ML, Baeyens B, Bradbury MH, et al.  
58  
59 769 Neof ormation of Ni phyllosilicate upon Ni uptake on montmorillonite: A kinetics study
- 60  
61  
62  
63  
64  
65



- 770 by powder and polarized extended X-ray absorption fine structure spectroscopy.  
771 Geochim Cosmochim Acta 2002;66:2335–47. [https://doi.org/10.1016/S0016-7037\(02\)00842-6](https://doi.org/10.1016/S0016-7037(02)00842-6).  
772
- 773 [50] Paineau E, Philippe AM, Antonova K, Bihannic I, Davidson P, Dozov I, et al. Liquid-  
774 crystalline properties of aqueous suspensions of natural clay nanosheets. *Liq Cryst Rev*  
775 2014;1:110–26. <https://doi.org/10.1080/21680396.2013.842130>.
- 776 [51] Grim RE. No Title. *Clay Mineral* 1968:464.
- 777 [52] Hamilton DL, Henderson CMB. The preparation of silicate compositions by a gelling  
778 method. *Mineral Mag J Mineral Soc* 1968;36:832–8.
- 779 [53] Robert JL, Beny JM, Della Ventura G, Hardy M. Fluorine in micas: crystal-chemical  
780 control of the OH-F distribution between trioctahedral and dioctahedral sites. *Eur J*  
781 *Mineral* 1993;5:7–18. <https://doi.org/10.1127/ejm/5/1/0007>.
- 782 [54] de Boer JH, Lippens BC, Linsen BG, Broekhoff JCP, van den Heuvel A, Osinga TJ. Thet-  
783 curve of multimolecular N<sub>2</sub>-adsorption. *J Colloid Interface Sci* 1966;21:405–14.  
784 [https://doi.org/10.1016/0095-8522\(66\)90006-7](https://doi.org/10.1016/0095-8522(66)90006-7).
- 785 [55] Horcas I, Fernández R, Gómez-Rodríguez JM, Colchero J, Gómez-Herrero J, Baro AM.  
786 WSXM: A software for scanning probe microscopy and a tool for nanotechnology. *Rev*  
787 *Sci Instrum* 2007;78. <https://doi.org/10.1063/1.2432410>.
- 788 [56] Dazas B, Lanson B, Delville A, Robert JL, Komarneni S, Michot LJ, et al. Influence of  
789 tetrahedral layer charge on the organization of interlayer water and ions in synthetic  
790 Na-saturated smectites. *J Phys Chem C* 2015;119:4158–72.  
791 <https://doi.org/10.1021/jp5123322>.
- 792 [57] Lanson B, Ferrage E, Hubert F, Prêt D, Mareschal L, Turpault MP, et al. Experimental  
793 aluminization of vermiculite interlayers: An X-ray diffraction perspective on crystal  
794 chemistry and structural mechanisms. *Geoderma* 2015;249–250:28–39.  
795 <https://doi.org/10.1016/j.geoderma.2015.03.005>.
- 796 [58] Jones RC. X-ray diffraction by randomly oriented line gratings. *Acta Crystallogr*  
797 1949;2:252–7. <https://doi.org/10.1107/s0365110x49000643>.

- 798 [59] Ferrage E, Lanson B, Sakharov BA, Drits VA. Investigation of smectite hydration  
799 properties by modeling experimental X-ray diffraction patterns: Part I.  
800 Montmorillonite hydration properties. *Am Mineral* 2005;90:1358–74.  
801 <https://doi.org/10.2138/am.2005.1776>.
- 802 [60] Ferrage E, Kirk CA, Cressey G, Cuadros J. Dehydration of Ca-montmorillonite at the  
803 crystal scale. Part I: Structure evolution. *Am Mineral* 2007;92:994–1006.  
804 <https://doi.org/10.2138/am.2007.2396>.
- 805 [61] Sun W, Rui X, Ulaganathan M, Madhavi S, Yan Q. Few-layered Ni(OH)<sub>2</sub> nanosheets for  
806 high-performance supercapacitors. *J Power Sources* 2015;295:323–8.  
807 <https://doi.org/10.1016/j.jpowsour.2015.07.024>.
- 808 [62] Brindley GW, Brown G. *Crystal Structures of Clay Minerals and their X-Ray*  
809 *Identification*. Mineralogical Society of Great Britain and Ireland; 1980.  
810 <https://doi.org/10.1180/mono-5>.
- 811 [63] Michot LJ, Bihannic I, Pelletier M, Rinnert E, Robert J-L. Hydration and swelling of  
812 synthetic Na-saponites: Influence of layer charge. *Am Mineral* 2005;90:166–72.  
813 <https://doi.org/10.2138/am.2005.1600>.
- 814 [64] Derkowski A, Kuligiewicz A. *Thermal Analysis and Thermal Reactions of Smectites: a*  
815 *Review of Methodology, Mechanisms, and Kinetics*. *Clays Clay Miner* 2023.  
816 <https://doi.org/10.1007/s42860-023-00222-y>.
- 817 [65] Franco F, Pérez-Maqueda LA, Pérez-Rodríguez JL. Influence of the particle-size  
818 reduction by ultrasound treatment on the dehydroxylation process of kaolinites. *J*  
819 *Therm Anal Calorim* 2004;78:1043–55. <https://doi.org/10.1007/s10973-005-0469-0>.
- 820 [66] Thommes M, Kaneko K, Neimark A V., Olivier JP, Rodriguez-Reinoso F, Rouquerol J, et  
821 al. Physisorption of gases, with special reference to the evaluation of surface area and  
822 pore size distribution (IUPAC Technical Report). *Pure Appl Chem* 2015;87:1051–69.  
823 <https://doi.org/10.1515/pac-2014-1117>.
- 824 [67] Jablonska B, Busch M, Kityk A V., Huber P. Natural and chemically modified post-  
825 mining clays — Structural and surface properties and preliminary tests on copper  
826 sorption. *Minerals* 2019;9:1–20. <https://doi.org/10.3390/min9110704>.

- 827 [68] Jin J, Zheng C, Yang H. Natural diatomite modified as novel hydrogen storage material.  
828 Funct Mater Lett 2014;7. <https://doi.org/10.1142/S1793604714500271>.
- 829 [69] Mondelli C, Bardelli F, Vitillo JG, Didier M, Brendle J, Cavicchia DR, et al. Hydrogen  
830 adsorption and diffusion in synthetic Na-montmorillonites at high pressures and  
831 temperature. Int J Hydrogen Energy 2015;40:2698–709.  
832 <https://doi.org/10.1016/j.ijhydene.2014.12.038>.
- 833 [70] Bardelli F, Mondelli C, Didier M, Vitillo JG, Cavicchia DR, Robinet JC, et al. Hydrogen  
834 uptake and diffusion in Callovo-Oxfordian clay rock for nuclear waste disposal  
835 technology. Appl Geochemistry 2014;49:168–77.  
836 <https://doi.org/10.1016/j.apgeochem.2014.06.019>.
- 837 [71] Sing KSW, Everett DH, Haul RAW, Moscou L, Pierotii RA, Rouquerol J, et al. Reporting  
838 physisorption data for gas/solid systems. Int Union Pure Appl Chem 1985;57:603–19.  
839 <https://doi.org/10.1351/pac198254112201>.
- 840 [72] Carrado KA, Csencsits R, Thiyagarajan P, Seifert S, Macha SM, Harwood JS.  
841 Crystallization and textural porosity of synthetic clay minerals. J Mater Chem  
842 2002;12:3228–37. <https://doi.org/10.1039/b204180b>.
- 843 [73] Horikawa T, Do DD, Nicholson D. Capillary condensation of adsorbates in porous  
844 materials. Adv Colloid Interface Sci 2011;169:40–58.  
845 <https://doi.org/10.1016/j.cis.2011.08.003>.
- 846 [74] Sarac Oztuna FE, Beyazay T, Unal U. Facile synthesis of graphene aerogel supported  
847 nickel/nickel oxide core-shell nanoparticles: efficient electrocatalysts for oxygen  
848 evolution reactions. J Phys Chem C 2019;123:28131–41.  
849 <https://doi.org/10.1021/acs.jpcc.9b07460>.
- 850 [75] Bastos-Neto M, Patzschke C, Lange M, Möllmer J, Möller A, Fichtner S, et al.  
851 Assessment of hydrogen storage by physisorption in porous materials. Energy Environ  
852 Sci 2012;5:8294–303. <https://doi.org/10.1039/c2ee22037g>.
- 853 [76] Panella B, Hirscher M, Roth S. Hydrogen adsorption in different carbon  
854 nanostructures. Carbon N Y 2005;43:2209–14.  
855 <https://doi.org/10.1016/j.carbon.2005.03.037>.

856 [77] Suh PM, Park HJ, Prasad TK, Lim D-W. Hydrogen storage in metal-organic frameworks.  
1  
2 857 Chem Rev 2012;112:782–835. <https://doi.org/10.1021/cr200274s>.  
3  
4  
5 858  
6  
7  
8  
9  
10  
11  
12  
13  
14  
15  
16  
17  
18  
19  
20  
21  
22  
23  
24  
25  
26  
27  
28  
29  
30  
31  
32  
33  
34  
35  
36  
37  
38  
39  
40  
41  
42  
43  
44  
45  
46  
47  
48  
49  
50  
51  
52  
53  
54  
55  
56  
57  
58  
59  
60  
61  
62  
63  
64  
65